NASA-CR-198020

ORIGINAL CONTAINS
COLOR ILLUSTRATIONS

ASSESSMENT OF CLIMATE VARIABILITY OF THE GREENLAND ICE SHEET:
INTEGRATION OF IN SITU AND SATELLITE DATA

K. Steffen, W. Abdalati, J. Stroeve, M. Stober, A. Nolin, J. Key
University of Colorado at Boulder
Cooperative Institute for Research in Environmental Sciences
Division of Cryospheric and Polar Processes
Campus Box 216, Boulder CO 80309

INTERIM
IN-45-CR
OCT
45503
P-41

NAGW-2158
Annual Progress Report
to
National Aeronautics and Space Administration

April 1995

Response of the Greenland Ice Sheet
to Climatic Forcing

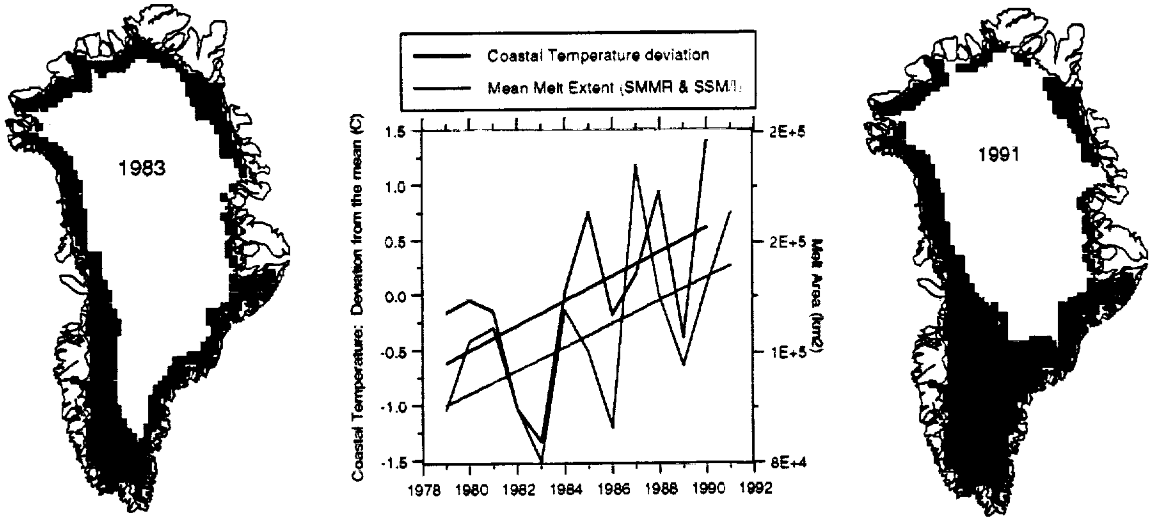

Satellite passive microwave-derived snow melt regions and climatological records from the coastal stations show the same warming trend for the Greenland ice sheet. Both data sets are based on the mean values for the melt season May through September.

(NASA-CR-198020) ASSESSMENT OF CLIMATE VARIABILITY OF THE GREENLAND ICE SHEET: INTEGRATION OF IN SITU AND SATELLITE DATA Annual Progress Report (Colorado Univ.) 41 p

N95-24846

Unclas

G3/45 0045503

Table of Contents

SUMMARY 1

1. INTRODUCTION 2

1.1 RATIONAL OF THE STUDY 2
1.2 LOGISTIC SUMMARY 2

2. SURFACE CLIMATOLOGY 3

2.1 OVERVIEW 3
2.2 RADIATION AND CLOUD REGIME 4
2.3 COMPARISON OF AERODYNAMIC PROFILE WITH EDDY CORRELATION 6
2.4 KATABATIC WIND CYCLES 7
2.5 ENGLACIAL TEMPERATURE 8

3. SURFACE ENERGY BALANCE MODELING 9

3.1 APPROACH 9
3.2 MODEL DESCRIPTION 9
3.3 TWO STREAM RADIATIVE TRANSFER MODEL 9
3.4 SNOWPACK MEASUREMENTS 10
3.5 RESULTS 10

4. SPECTRAL BIDIRECTIONAL REFLECTANCE OF SNOW 12

4.1 APPROACH 12
4.2 DESCRIPTION OF THE MODEL 12
4.3 FIELD MEASUREMENTS 12
4.4 RESULTS 13

5. AVHRR TIME SERIES 14

5.1 INTRODUCTION 14
5.2 GREENLAND ICE SHEET VARIATIONS 15
5.3 OUTGOING LONGWAVE RADIATION 15
5.4 NET ALL-WAVE RADIATION 15
5.5 TIME SERIES AT THE ETH/CU CAMP 15
5.6 TIME SERIES AT THE SUMMIT 16

6. ATSR CASE STUDY 18

6.1 INTRODUCTION 18
6.2 SURFACE TEMPERATURE RETRIEVAL 18
6.3 APPLICATION TO AND ATSR SCENE 19
6.4 CLOUD DETECTION 21
6.5 COMPARISON WITH AVHRR 21

7. SURFACE MELT 22

7.1 SURFACE OBSERVATIONS 22
7.2 PASSIVE MICROWAVE MELT ASSESSMENT 23
7.3 PASSIVE MICROWAVE MELT ALGORITHMS: LIMITATIONS 25

8. SMMR AND SSM/I-DERIVED SNOW ACCUMULATION 27

9. REFRACTION AND ICE MOVEMENTS 28

9.1 INTRODUCTION 28
9.2 REFRACTION 29
9.3 ICE MOVEMENTS AND DEFORMATIONS 32

10. REFERENCES 38

SUMMARY

In 1994 we completed a successful field season at the ETH/CU camp on the Greenland ice sheet. The major accomplishments were:

- Retrieval of 305 days of climate and glaciological data recorded in our absence.
- First year-round net radiation balance and short-wave radiation balance recordings.
- A height diminution in the last 3 years of -0 20 $m\ y^{-1}$ was measured for the ice surface in the vicinity of the camp. This agrees well with measurements from the EGIG-line.
- The average displacement at the ETH/CU camp is 0.3196 $m\ d^{-1}$, the velocities and the flow azimuth are not completely homogeneous.

Data analysis showed the following results:

- Cloud classification based on longwave sky radiation revealed that overcast sky occurred for 25% of the time in winter, and for 15% in spring and summer respectively. Winter and summer both show the same occurrence of clear sky of approximately 26%.
- Comparison of aerodynamic profile method with eddy correlation method to derive sensible and latent heat flux showed good agreement in the diurnal cycle. The turbulent fluxes were underestimated with the aerodynamic method by 10 - 30% as compared to the *in situ* eddy flux method.
- The katabatic wind shows a distinct diurnal cycle with a maximum in the morning (7-9 h solar time) and a minimum in the late afternoon (18 h solar time).
- Snow grain size was modeled with a surface energy balance model (SNTHERM) and compared with in situ measurements. Sharp decreases in the modeled snow grain size, caused by accumulation events such as precipitation and deposition, could be verified with observational data.
- Radiative transfer modeling of firn support our beliefs that the observed trends in 18 and 19 GHz passive microwave brightness temperatures are attributable to accumulation rate changes. Modeling also indicates the above relationship is detectable because of the presence of depth hoar.
- Snow melt can be detected by a distinct signal in the passive microwave cross-polarized gradient ratio (19h-37v)/(19h+37v) and has been used for wet/dry snow classification.
- Top of the atmosphere (TOA) broadband albedos were derived from AVHRR visible and near infrared reflectances for the entire ice sheet from May 1990 - June 1991. The highest albedo values are found along the southeast coast of the ice sheet which is consistent with the summer peak of precipitation due to onshore flow loaded with high water vapor content. TOA albedo values dropped to around 40% along the south-western coast during July and August due to bare ice surface.
- The net all-wave radiation balance at the top of the atmosphere is negative over the entire ice sheet except for the summer month June-July-August. In June, the net radiation balance is slightly positive over the dry snow areas (15 W/m2).

1. Introduction

1.1 Rational of the Study

The proposed research involves the application of multispectral satellite data in combination with ground truth measurements to monitor surface properties of the Greenland Ice Sheet which are essential for describing the energy and mass of the ice sheet. Several key components of the energy balance are parameterized using satellite data and *in situ* measurements. The analysis will be done for a ten year time period in order to get statistics on the seasonal and interannual variations of the surface processes and the climatology.

Our goal is to investigate to what accuracy and over what geographic areas large scale snow properties and radiative fluxes can be derived based upon a combination of available remote sensing and meteorological data sets. Operational satellite sensors are calibrated based on ground measurements and atmospheric modeling prior to large scale analysis to ensure the quality of the satellite data. Further, several satellite sensors of different spatial and spectral resolution are intercompared to access the parameter accuracy. Proposed parameterization schemes to derive key component of the energy balance from satellite data are validated. For the understanding of the surface processes a field program was designed to collect information on spectral albedo, specular reflectance, soot content, grain size and the physical properties of different snow types. Further, the radiative and turbulent fluxes at the ice/snow surface are monitored for the parameterization and interpretation of the satellite data.

The expected results include several baseline data sets of albedo, surface temperature, radiative fluxes, and different snow types of the entire Greenland Ice Sheet. These climatological data sets will be of potential use for climate sensitivity studies in the context of future climate change.

1.2 Logistic Summary

We arrived at the ETH/CU camp on April 18, 1994 and the station was occupied until June 14, 1994. The following members took part in the 1994 field expedition:

Name	*Institution*	*Arr.*	*Dep.*
Konrad Steffen	CU-Boulder	5-25	6-14
Anne Nolin	CU-Boulder	4-18	5-25
Waleed Abdalati	CU-Boulder	4-18	6-14
Jason Box	CU-Boulder	4-18	6-14
Jay Zwally	GSFC-NASA	5-25	6-14
Manfred Stober	FHS Stuttgart	5-25	6-14
Jürgen Kreutter	FHS Stuttgart	5-25	6-14

We retrieved climatological and glaciological data recorded in our absence for 305 days. All sensors worked for the entire time period and there was no data loss. For the first time radiation data for shortwave incoming and reflected and net radiation was recorded throughout the winter and the data analysis presented in Chapter 2.2 showed promising results and applications. In general, the field season was much colder than the previous years with only a few days at or above 0° C. The temperature recording at the ETH/CU camp showed a decrease of the mean air temperature from -10° C to -13° C for the time period 1991 - 1994. The general cooling trend at the ETH/CU camp coincides with the large scale cooling trend observed for the southwestern part of the Greenland ice sheet for the winter months based on the coastal station data.

2. Surface Climatology

2.1 Overview

For 47 consecutive days during the 1994 field season, continuous measurements were made of 30 climatological parameters (Table 2.1 and 2.2). Also, continuous records of a 10 m temperature and wind speed profile, and a 10 m ice thermal profile, started in mid 1991 was collected and maintained (Table 2.3). The separate components of the radiative energy balance were measured as described in the tables below. Latent and sensible heat fluxes were obtained by eddy correlation measurements and also from the bulk aerodynamic profile method.

Problems arose with the eddy correlation measurements due to the fragility of the finewire temperature sensor which has a diameter of 6.6×10^{-6} m. While the small mass allows the fine wire to react quickly to the temperature structure of passing eddies, the sensor is left quite vulnerable to airborne ice crystals. As a consequence, we have four eddy correlation datasets of limited temporal coverage. For the majority of measurements, digital sampling occurred each 10 seconds, this data was then averaged every 10 minutes and written to final storage. The mean 2-m air temperature at the ETH/CU camp was -6.03° C with a mean wind speed of 6.75 ms^{-1} for the time period April 15 to June 11, 1994.

Table 2.1 Radiation Individually measurement of all components of the radiative energy balance

Measured Component	*Instrument type*	*misc. info.*
R_n (net radiation)	REBS	0.3 - 60 μm response
S↓ (incoming shortwave	Eppley Pyranometer	0.3 - 3 μm response
S↓ (incoming diffuse shortwave)	Eppley Pyranometer	- Shade rings used to obtain diffuse measurements
S↑ (reflected shortwave)	Eppley Pyranometer	- on boom arm
L↓ (*diffuse* downwelling longwave radiation)	Eppley Pyrgeometer	4 - 50 μm response
S_d direct solar beam component	Eppley Pyrheliometer	- on solar tracker.
$S_{d\lambda}$ Sun photometer with narrow-band spectral filters in Visible and Near IR.	*EG&G* sensitive photoelectric diodes	- on solar tracker - 442, 550, 600, 880, 940 nm interference filters.

Table 2.2 Turbulent Flux Measurements (Sensible and Latent Heat)

Measurement method	*Sensor info.*	*misc. info..*
Eddy Correlation	- Krypton UV Hygrometer (10 Hz response) - CA 127 sonic anemometer with fine-wire thermocouple (10 Hz response). - barometric pressure (SB 270). - temperature and relative Humidity	- limited record - fast response instruments recording @ 5 Hz, average over 10 minutes.
Aerodynamic Profile	- 3 level profile of: temperature; humidity; and wind (RH-207 & Met-One 3-cup anemometers).- 0.54, 1.04, 2.04 m levels. - barometric pressure (SB 270)	- continuous record - April 15 - June 15

Table 2.3 Measurements running from mid 1991 unless otherwise noted

Measurement	*Sensor*	*misc. info.*
10 M tower profile		
S* (SW radiation balance: 2 x S↓; 1 x S↑. (albedo))	3 x Li-Cor photoelectric diodes	mid 1993 to present 1 hour temporal resolution 0.4 - 1.2 μm spectral response
R_n (net radiation)	REBS (0.3 - 60 μm)	mid 1993-present 1 hour temporal resolution
temperature profile		height: 2 m; 10 m
wind profile		mid 1994 to present height: 2 m; 8 m
wind direction		height: 10 m
barometric pressure	SBP 270	mid 1994 - present
Snow thermal profile		
	fine-wire thermocouples	June 1994 to present - positioned at: surface; 0.05 m; 0.1 m; 0.2m; 0.35m; 0.50 m; 0.65 m 0.9 m ice interface
10m ice thermal profile		
		- number of measurements - depths

2.2 Radiation and Cloud Regime

The shortwave and net radiation balance was measured for the first time throughout summer and winter (Fig. 2.1). Unattended radiation measurements have been problematic in the past with conventional pyranometers due to icing of the quartz dome. We used Silicon-device pyranometers due to its small size and mass. Because of the constant katabatic wind the snow accumulation on the sensors was not a problem. First data analysis showed that the two upward looking pyranometers, the downward looking pyranometer, and the net radiometer provided good results. For eight consecutive months (Oct. through April) the net radiation balance is negative or zero (Fig. 2.1). The net radiation values at or close to zero Wm^{-2} represent low and mid-level cloud cover during the winter months. The month of July showed the largest positive net radiation, which also coincides with the largest ablation rates at the snow surface.

A cloud classification algorithm has been developed based on synoptic observations and longwave sky radiation measured in spring 1993. The 3-hourly synoptic cloud observations were coded according to the cloud cover between 0 and 8. The comparison between the longwave sky radiation from radiative active clouds such as stratus and altos clouds and the synopic cloud code showed that cloud fractions can be classified within 10% accuracy. Cirrus clouds can not be detected with this radiation method because of their cold temperature of approximately -50° C. The cloud fraction algorithm has been applied to the radiation set collected during winter 1993/94 and spring 1994. The analysis shows overcast sky conditions for 26% that during winter and spring, and clear sky conditions of 24% in spring, 15% in winter respectively (Fig. 2.2). This data set can be used for cloud detection, especially during the polar night when satellite cloud detection is most inaccurate. This method will be applied in future to the forthcoming Greenland climate monitoring network station data and should provide an year-round cloud statistic baseline data set for future satellite altimeter measurements.

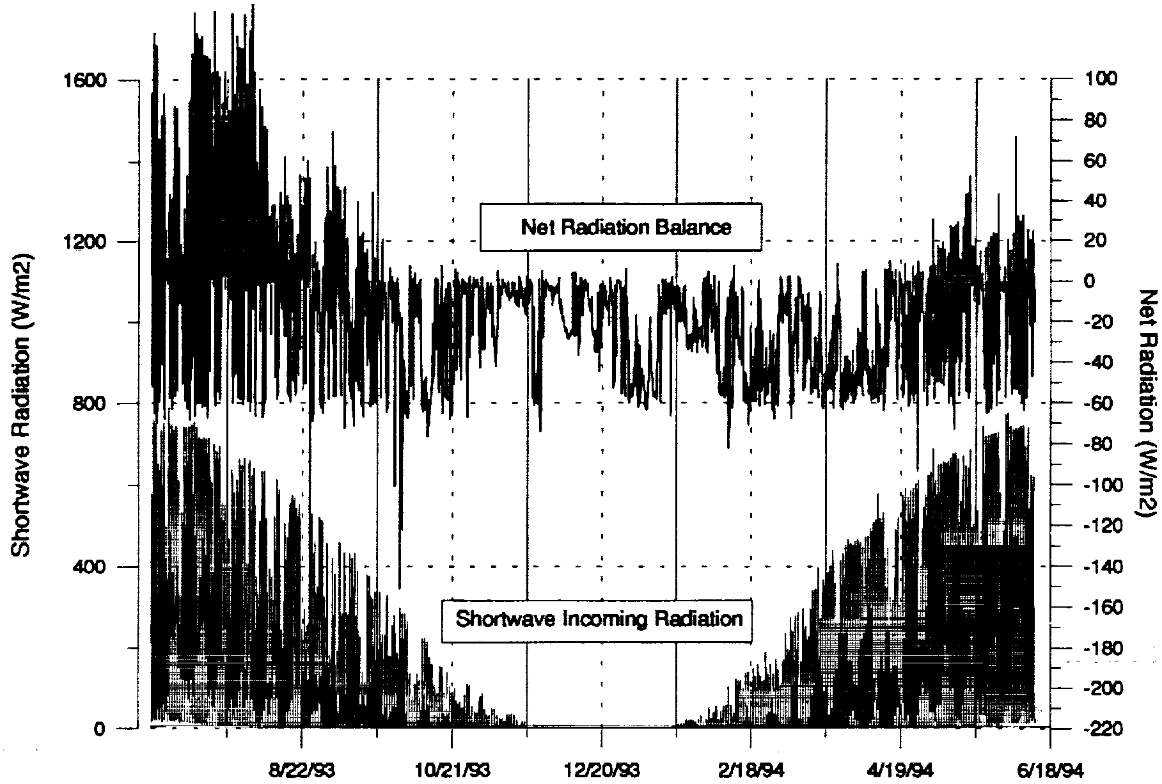

Figure 2.1: Annual cycle of shortwave incoming radiation and net radiation at theETH/CU camp.

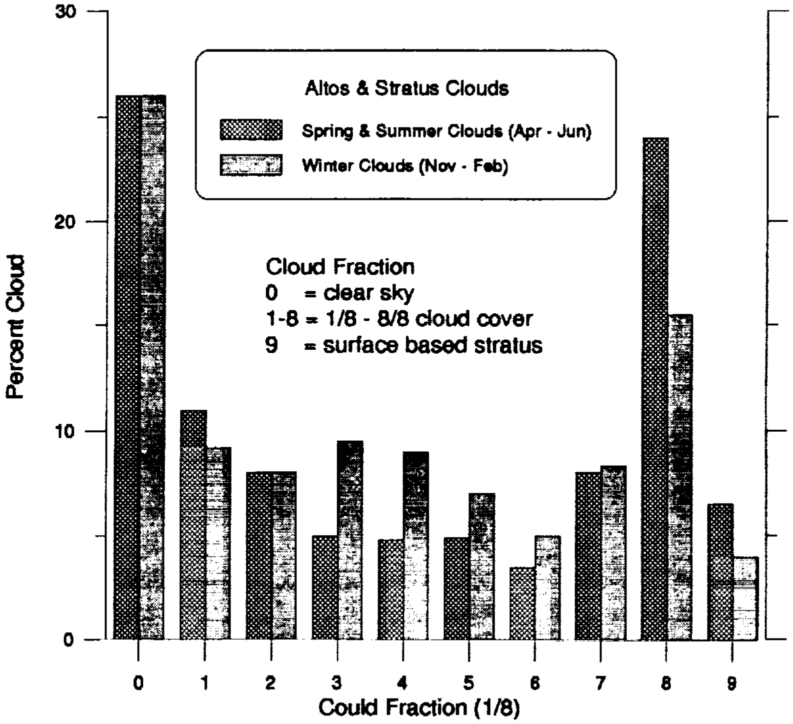

Figure 2.2: Could amount classification for low and mid-level clouds (Stratus and Altos clouds) at the ETH/CU camp for two time periods in Nov. 93 - Feb. 94, and Apr. - June 94. The classification of the cloud statistics is based on longwave sky radiation measurements.

2.3 Comparison Of Aerodynamic Profile with Eddy Correlation

Following is a discussion of two methods to derive sensible and latent heat fluxes in the surface boundary layer, the *Aerodynamic Profile method (APM)* and the *Eddy Correlation method (ECM)*. The eddy correlation uses fast response instrumentation to measure the sensible, hygric, and kinematic structure of passing eddies. To resolve the structure of the eddies at 1.0 m, the sampling rate must be 5-10 Hz. The APM includes the measurement of vertical gradients of temperature, humidity, and wind on a profile.

Our plan to employ the use of the APM for the network of automatic weather stations on the Greenland ice sheet requires that we have a detailed understanding of the boundary layer stability and its turbulent eddy structure. The APM uses stability criteria that are based on experimental measurements in the mid latitude and over vegetated surfaces. We have run both methods coincidentally on the Greenland ice sheet to compare the relative accuracy of the APM to the ECM. The ECM is considered to provide accurate turbulent flux measurements (Figure 2.3). The APM assumes neutral stability in the boundary layer. Though this is not always the case, the calculated fluxes can be scaled by a stability parameterization derived from a comparison of the two methods.

The APM is currently the best suited for automatic / long-term sensible and latent heat flux measurements on the Greenland ice sheet. The ECM is not practical for long-term automatic measurements, because the instrumentation needs continuous supervision. The ECM instrumentation is highly susceptible to damage in snowstorms and other adverse conditions.

When both methods are run coincidentally, a quantitative comparison can be made. The two methods agree well under specific conditions. The APM calculations improved through comparison. Specifically, it is the stability functions that can be tuned to fit the micro-meteorological conditions of Greenland that the APM uses to derive turbulent fluxes.

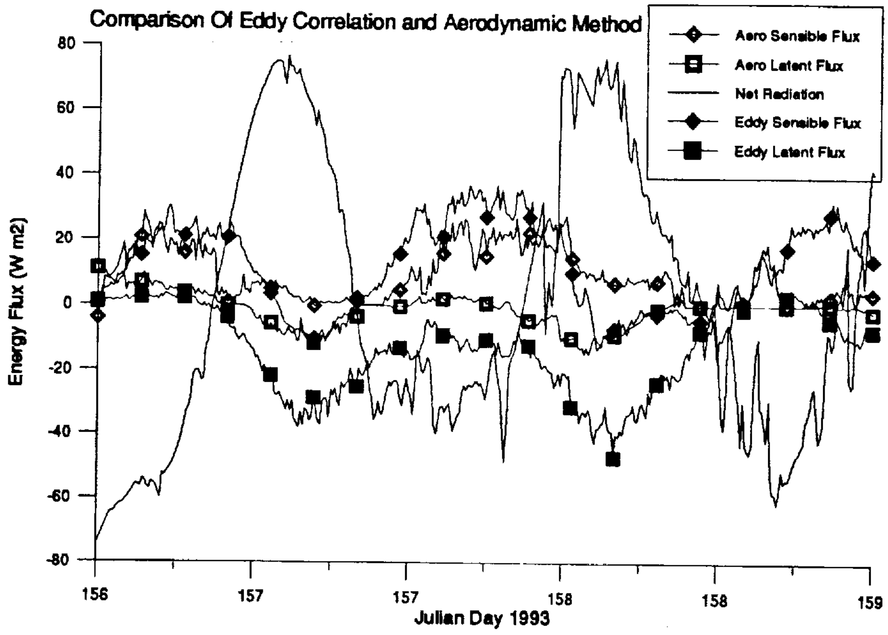

Figure 2.3: Time series comparison of turbulent flux measurements derived from the eddy correlation method and the aerodynamic profile method with net radiation. Aerodynamic profile data has solid points, eddy correlation are hollow.

2.4 Katabatic Wind Cycles

The katabatic, cold air drainage wind, has a diurnal cycle driven by radiation and subsequent thermal forcing. Under normal conditions, *i.e.* no strong synoptic scale influence, the diurnal cycle of cold air drainage down the ice sheet was observed to exhibit remarkable periodicity. Our measurements show that the wind frequently has a maximum in the morning 0.25-0.45 *solar time* (ST) , weakens through mid-day and reaches a minimum in the late afternoon 0.7-0.8 ST. Figure 2.4 represents the time of maximum daily wind speeds. The daily wind maximum and the minimum (not shown here) occurred frequently within the same time interval, indeed several times within the same 10 minute interval as another day. In the first 28 days, there were 4 instances where 2 days had the same 10 minute interval for the daily minimum wind speed.

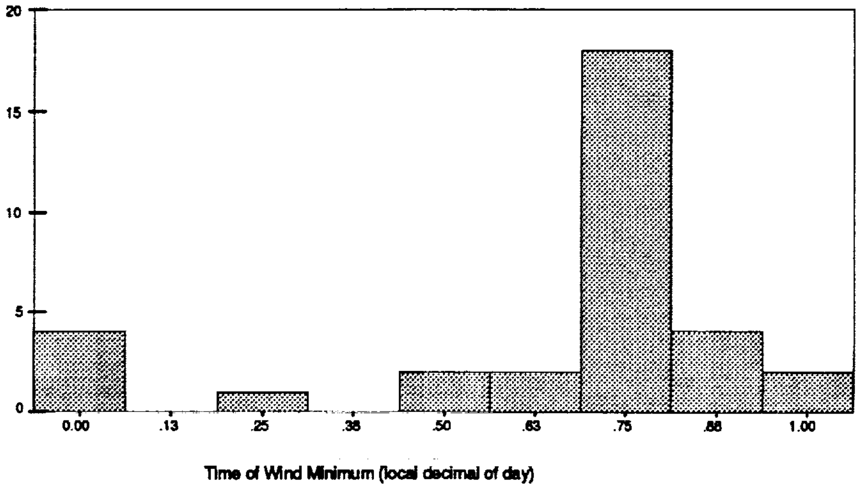

Figure 2.4: Histogram of daily decimal time of wind maximum. Cases are taken where flow is considered katabatic from within ~22° of 135° from true north.

The annual wind direction data show the dominance of the katabatic flow (Fig. 2.5). For a 12 month measuring period, approximately 63% of the time the wind came from 135±22 degrees.

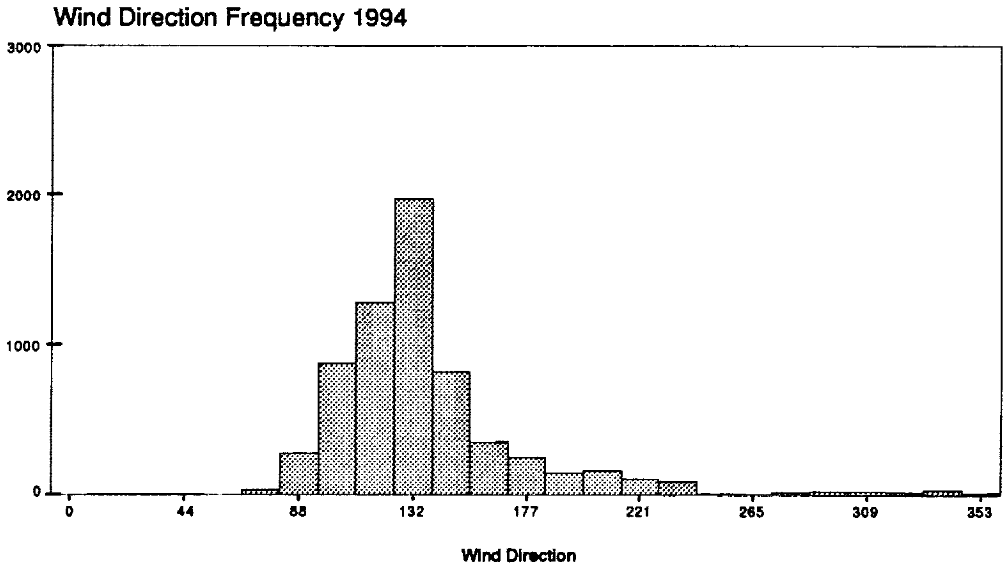

Figure 2.5: Histogram of 10 minute temporal resolution wind direction data from 1994 field season (April 15-June 11).

2.5 Englacial Temperature

The ice temperature was measured with thermistors (Fenwal type: Unicurve UUB31J1) having an accuracy of ±0.2° C. The mean 10 m ice temperature was -8.6° C with a standard deviation of ±0.3° C (Fig. 2.6), the 9 m ice temperature was -8.7° C with a standard deviation of ±0.4° C. The ice temperature between 10 and 50 m depth varies only by 0.2° C (measurements from the 650 m deep GGU thermistor readings at the ETH/CU camp in 1990). The mean ice temperature at 10 m depth from the 1994 measurements gave the same value (within 0.1° C) as compared to the 1991 measurement. The mean air temperature for the ETH/CU camp for the same time period is -13.3° C (1.7 m above the snow surface). It is not clear why the mean 10 meter ice temperature and the mean air temperature were approximately 5° C apart. In general, it is assumed that the 10 m ice temperature provides a good proxy value for the mean air temperature. A possible explanation is the release of heat due to water percolation through the snow cover and refreezing at the glacier ice. The annual snow cover did not melt at the ETH/CU camp for the past three years, and an "aufeis" layer of 0.6 m thickness was observed. The release of energy from the percolating melt water could have increased the overall ice temperature to a depth of 10 m. This phenomena will be studied further and the energy input will be modeled.

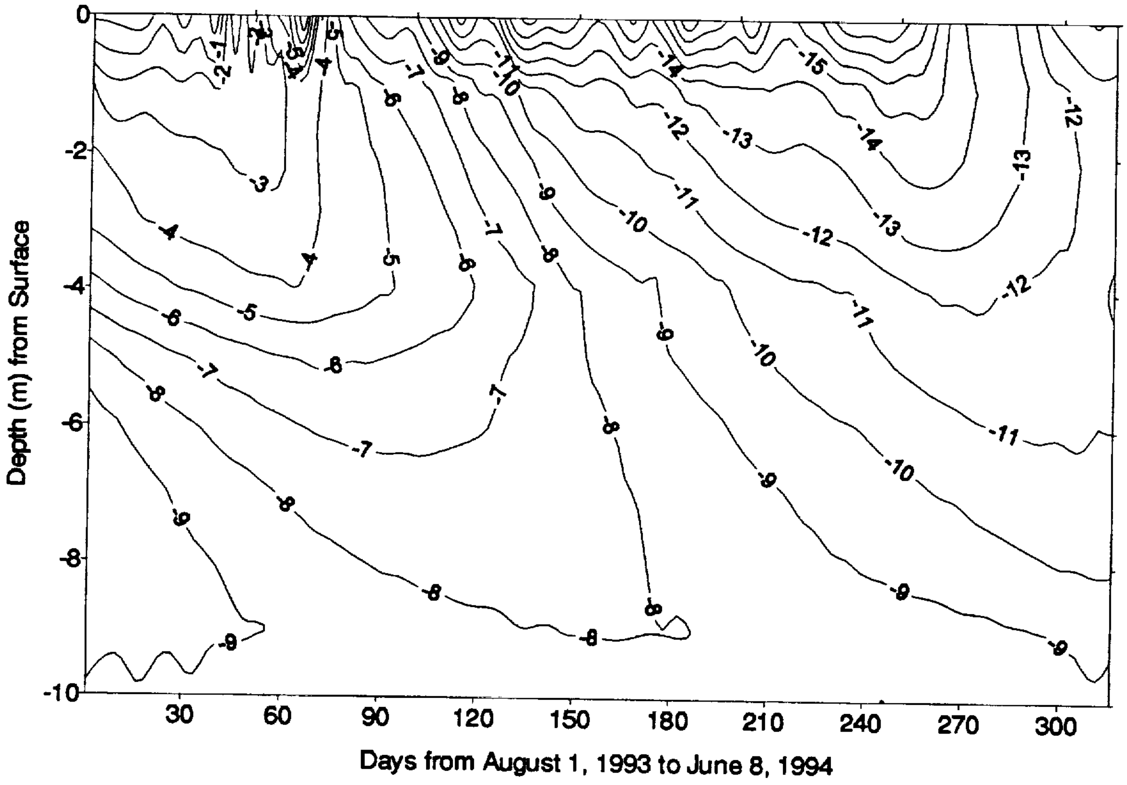

Fig. 2.6 *Evolution of englacial temperature profile at the ETH/CU camp for a 10-month period. The thermistor chain was inserted into the ice in spring 1990. The ice temperature was recorded at 1 meter interval to a depth of 10 m.*

3. Surface Energy Balance Modeling

3.1 Approach

To examine the relationship between snowpack energy balance, snow grain size, a one-dimensional model energy and mass fluxes in snow was used to calculate snow grain size as a function of meteorologic variables. From these grain size data, the radiation scattering and absorbing properties of snow can be calculated using Mie theory. These optical properties are then used as input to a two stream radiative transfer model that calculates the spectral albedo.

3.2 Model Description

The SNTHERM model (Jordan, 1991) takes as input values of air temperature, relative humidity, wind speed, air pressure, incoming and outgoing shortwave radiation, incoming longwave radiation, and precipitation information at regular time steps (in this case, every 10 minutes). Snow accumulation data (accumulation rate and grain size) were obtained from a combination of synoptic weather observations (every 3-6 hours), grain size measurements and additional field observations.

The model was initialized with snowpack physical data including grain size, temperature and density (from field measurements). It then generated a time series of snowpack temperature, grain size and density profiles corresponding to the time intervals of the input meteorologic data.

The model uses a grain growth algorithm based on Colbeck's formulation (Colbeck, 1983) for metamorphism in dry snow:

$$\frac{\partial d}{\partial t} = \frac{gl}{d} D_{e0s} \frac{1000}{P_a} \left(\frac{T}{273.15} \right)^6 C_{kT} \frac{\partial T}{\partial z} \tag{3.1}$$

where d is snow grain diameter (m), gl is a grain growth parameter, D_{e0s} is the effective diffusion coefficient for water vapor, P_a is atmospheric pressure (mb), T is snow temperature (K), C_{kT} is the variation of saturation vapor pressure with temperature and z is the height (m) above the snow-ice interface. A separate formulation is used for grain growth in wet snow but during the experiment period, May 2 to 25, 1994, there was no significant snow melt. Thus, the complicating effects of liquid water on grain growth (Colbeck, 1973) were avoided. Because albedo is affected by grain size in the top few centimeters of the snowpack, only measurements of the surface layer grain size needed to be considered.

3.3 Two stream Radiative Transfer Model

Using the snowpack physical properties grain size, depth and density, the optical thickness, single scattering albedo and asymmetry parameter were calculated. The single scattering albedo represents the probability that light incident on a particle will be scattered rather than absorbed. The resulting direction of the scattered light is described by the scattering phase function of a particle P(θ), where θ is the scattering angle. The asymmetry parameter, g, is a parameterization of the particle scattering phase function. In this case, because the snowpack was thick enough to be considered "optically-thick" (where the substrate has virtually no effect on albedo), the optical thickness, a dimensionless number, was prescribed to be 1000. Both the single scattering albedo and asymmetry parameter are functions of grain size and so were determined using the SNTHERM model output values. From these input values, the twostream model calculated the directional-hemispherical reflectance at the top of the snowpack.

3.4 Snowpack Measurements

Snow grain size was measured 11 times over the model run period. A gridded card and hand lens were used to measure the maximum, minimum and mean grain size for replicate samples of snow from the top 5 cm of the snowpack. Six snowpits were excavated to provide density and snow stratigraphy information as well. Snowpack reflectance was measured using a portable field spectrometer that operates in the 400 to 2500 nm spectral range. These reflectance values were collected for comparison with the albedo estimates calculated from the radiative transfer model. To initialize snowpack temperature in the snowpack energy and mass balance model, temperature data were acquired from thermistor and fine-wire thermocouples placed in the snowpack.

3.5 Results

For the period from May 2 to May 25 the SNTHERM model generated the snow surface layer grain size data that could then be compared with measurements of snow grain size from the same period. Figure 3.1 shows good agreement the mean measured grain size (boxes) and the modeled grain size (solid line).

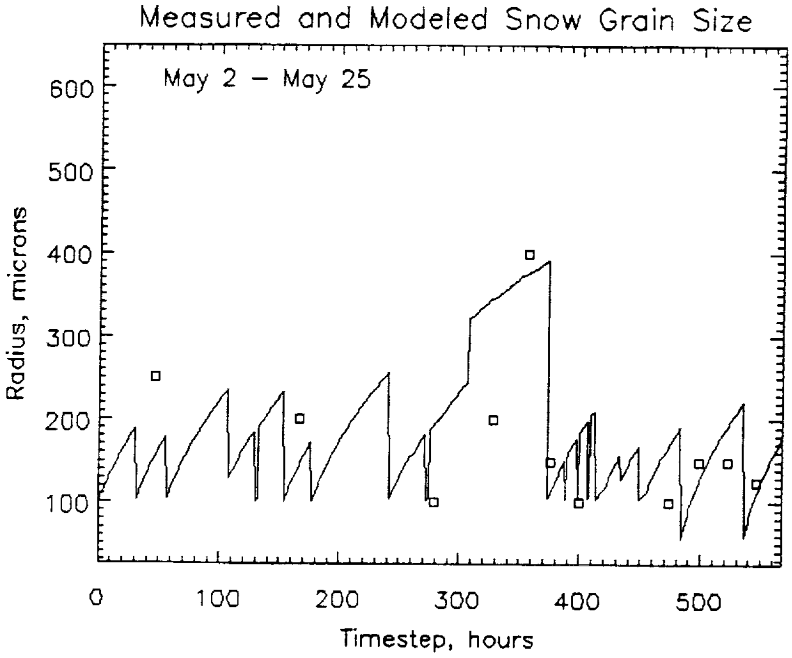

Figure 3.1: Comparison of both modeled (solid line) and measured mean snow grain radius (boxes) for the experiment period from May 2 - May 25, 1994. Sharp decreases in the modeled snow grain size were caused by accumulation events such as precipitation and wind deposition.

The irregular, sharp dips in modeled grain size are the result of snow accumulation episodes, mostly from blowing and drifting snow but also from precipitation. Following an accumulation event, the surface snow grains showed steady increases in size as metamorphism proceeded in the snowpack. While the maximum and minimum grain size measurements have a wide range (see Table 3.1), the mean grain size closely tracks changes in modeled grain size.

Table 3.1: Measured grain sizes from the snowpack surface

Minimum radius (µm)	Mean radius (µm)	Maximum radius (µm)
100	250	500
100	200	550
50	100	175
100	200	500
100	400	1250
100	150	300
50	100	250
50	100	300
50	150	350
100	150	400
75	125	350

Comparing the modeled albedo values with field reflectance data (Figures 3.2) provides an additional check on the method. For May 9, 1994, the measured reflectance is slightly lower in the visible region and slightly higher in the near-infrared region than the modeled data. This may be due because the model assumes spherical grains and the surface grains tended to be somewhat dendritic, comprised of broken crystals. There is some noise present in the measured field reflectance spectrum, particularly in the .8 - 1.0 µm region (low signal-to-noise response of the spectrometer). However, for the most part, the near-infrared spectra match well. Since the measured spectra do not represent the energy distribution integrated over the upward hemisphere, one would not expect it to exactly correspond with the modeled albedo.

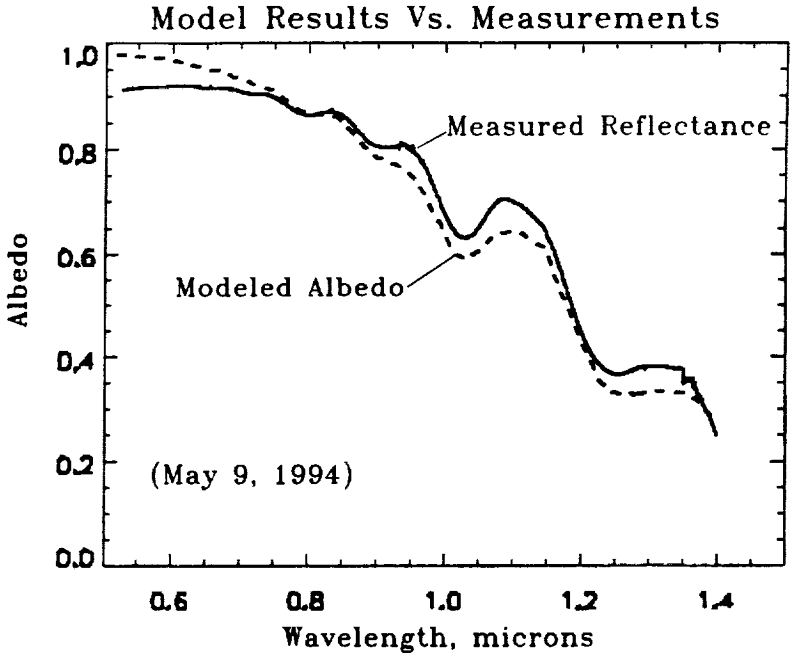

Figure 3.2: May 9, 1994; measured spectral reflectance (field spectrometer) and modeled albedo (twostream radiative transfer model). Measurements are shown with the solid line and model results are shown with the dashed line. Mean measured grain radius was 200 µm.

4. Spectral Bidirectional Reflectance of Snow

4.1 Approach

A combination of field measurements and model data were used to generate information about the spectral bidirectional reflectance of snow. Snow reflectance measurements were acquired and corresponding snowpack physical properties, including depth, density and grainsize, were measured.

4.2 Description of the Model

The discrete-ordinate model (Stamnes, 1988) was used to calculate spectral directional reflectance as a function of the optically equivalent ice grain radius. Optical parameters needed for the discrete-ordinate model include snowpack optical thickness, single scattering albedo, and asymmetry parameter (or a description of the scattering phase function); these are calculated from the snowpack physical properties: depth, bulk density and equivalent grain size. Diffuse irradiance, substrate reflectance, and solar and viewing geometries are also required as model inputs. For semi-infinite snowpacks, density has a negligible effect on snowpack reflectance (Bohren, 1979) leaving grain size as the property that exerts the greatest control over near-infrared reflectance.

To compare with the reflectance factor measurements, the discrete-ordinates model was run using the same solar and viewing geometries and snowpack physical properties as for the measurements. The model requires as input the snowpack optical properties which were derived from the physical properties using the equations of Mie theory and the refractive indices for ice (Warren, 1984). Since the snowpack is considered to be an optically semi-infinite medium, in which the substrate reflectance does not influence the reflectance from the snowpack, the optical thickness value used in the model can be some arbitrarily large value. In this case, an optical thickness value of 1000 was used.

4.3 Field Measurements

Spectral and angular reflectance measurements were made using a portable field spectrometer with a spectral range from 350-2500 nm. The instrument has 350 spectral bands in the ultraviolet and visible wavelengths (350-700 nm) and 1801 channels in the near-infrared wavelengths (700-2500 nm), with 1 nm spectral resolution throughout the entire spectral range. However, because of low a signal-to-noise ratio in the ultraviolet and part of the near-infrared region, only data within the spectral range from 400-1750 were used.

A fiber optic bundle serves as the sensor head allowing for flexibility in maneuvering for angular measurements. The tip of the fiber optic was mounted in a pistol grip, the base of which was mounted on a rotating tripod head. The tripod head could be moved in both nadir and azimuthal directions and fixed at specified angles. To limit the angular field-of-view of the fiber optic, an 8 deg foreoptic was attached to the sensor head. Measurements were made from 0 deg (looking straight down) to 75 deg, in 15 deg increments in the nadir direction and from 0 deg (looking towards sun) to 180 deg, in 15 deg increments in the azimuthal direction. Because of the change in viewing zenith and the fixed height of the instrument, the geometry of the instrument setup did not allow the same size snow area to be viewed for each measurement. However, because of the homogeneous nature of the snow, this was not considered a problem. Reflectance data were acquired by first collecting a reflectance spectrum from a sunlit calibrated spectralon reference panel and then collecting a snow spectrum. Each measurement was actually an average of ten rapidly acquired spectra for both the spectralon and snow. The ratio of the averaged values was automatically calculated and stored. A full set of angular measurements could be acquired in a 20-30 minute period.

Measurements of snow grain size and snow bulk density were made at the time of the reflectance measurements so that snow optical and physical properties could be related. Adjacent to the site of each set of reflectance measurements, snow samples were removed by spatula from the side of each snow pit and carefully desaggregated onto a gridded metal plate Snow grain diameters were estimated by eye using the gridded card and magnifying loop. Maximum, minimum, and mean radius were estimated and a minimum of two replicates were performed for each grain size estimate. Grain size determinations were made for the near-surface layer (typically 0-3 cm) and for 10 cm intervals to a depth of 50 cm.

Though the model results are not dependent on bulk density when the snowpack is optically semi-infinite (when the substrate does not affect the modeled reflectance), it was possible that density variations may in some way influence the angular reflectance. Thus, these data are presented for completeness. Snow bulk density was measured by collecting snow samples of known volume and weighing them using a spring balance. Samples were collected from the side of each snow pit at 10 cm intervals. Replicate samples were collected and averaged for each snow depth.

4.4 Results

Snow conditions differed for the three measurement days May 9, 1994 had homogeneous, wind-packed snow 0-10 cm layer with a mean grain radius of 200 µm. On May 17, 1994, the surface layer of the snowpack was refrozen suncrust and sintered grain clusters with a mean grain radius of 400 µm. The snowpack on May 24, 1994 was again fine-grained windpack with a mean grain size of 150 µm.

The spectral reflectance measurements demonstrate the strong forward scattering from the snowpack for all three days of measurements. Figure 4.1 shows the reflectance measurements from May 17th. The forward scattering peak is greater for the coarse-grained refrozen sun-crusted snow than for the finer-grained windpack. This is expected since larger ice particles have a larger value for the asymmetry parameter, g, meaning more that they are more forward scattering.

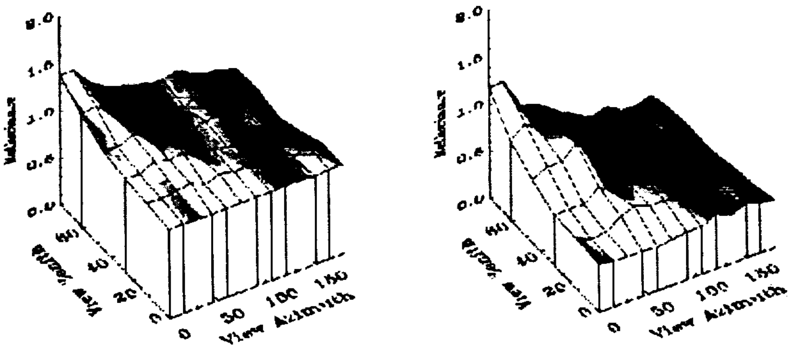

Wavelength = 0.46 um **Wavelength = 1.03 um**

Figure 4.1: May 17, 1994. Angular reflectance measurements of coarse-grained, refrozen suncrusted snow. Mean surface layer grain size was 400µm.

There is no evidence of a backscatter peak though this may be more a function of the surface micro-topography than lack of an opposition effect. Surface roughness appears to play an important role. The proportion of the field-of-view occupied by shadows increases as the relative azimuth decreases and as the viewing zenith increases. The same would be true as the solar zenith angle increases. Also, surface micro-topography changes the effective solar zenith angle.

Model results (Figures 4.2) predict a higher degree of forward scattering than is seen in the measurements.

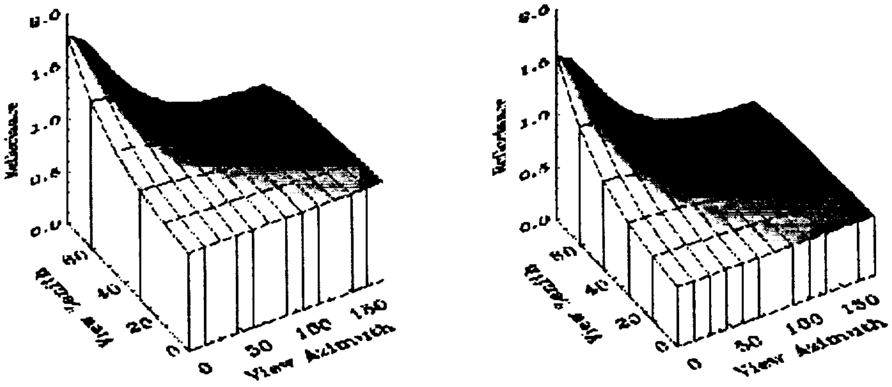

Wavelength = 0.46 um

Wavelength = 1.03 um

Figure 4.2 : Discrete-ordinate model results using the same grain size as for May 17, 1994.

This discrepancy between measurements and model results may be due to several factors. Surface roughness is not accounted for in the model and, as noted above, appears to be important for measurements made near the snow surface. Deviation of the calibrated reference panel from the cosine law may also lead to underestimation of measured reflectance at low sun angles. At very low sun angles, fewer photons are experiencing multiple scattering events so that the problem becomes one of single-scattering rather than solely a multiple scattering phenomenon. Lastly, the asymmetry parameter is not a complete description of the particle scattering phase function and may provide a good representation of the angular distribution of reflected energy. However, computational and model limitations currently prevent calculation and use of the full particle phase function.

5. AVHRR Time Series

5.1 Introduction

The variation of outgoing longwave radiation emitted (OLR) and solar radiation reflected at the top of the atmosphere provides a measure of the total energy balance of the earth-atmosphere system and is a key factor in the understanding of climate change. Unlike surface radiative fluxes, satellites provide the only direct measurements of these variables.

Using results from NOAA-11 Advanced Very High Resolution Radiometer (AVHRR) Global Area Coverage (GAC) data, the spatial and temporal variations of the net longwave, net shortwave, and net all-wave radiation at the top of the atmosphere (TOA) are calculated for the Greenland ice sheet from May 1990 - June 1991. All data analyzed are at around 1500 GMT (near local noon).

5.2 Greenland Ice Sheet Variations

TOA broadband albedos were derived from AVHRR visible (VIS) and near infra-red (NrIR) reflectances using Li and Leighton's (1992) conversion for snow/ice. These albedos show that 1990 was a relatively warm year and that the melt season extended well into August. Along the south-western coast the area covered by bare ice increases substantially from June to August as shown by monthly TOA albedo values dropping to around 40%. Also observed is an increase in the melt area from June to August along the western coast and also in the north-eastern part of Greenland as well as a smaller area in the north-western part of Greenland. Daily variations in albedo further suggest that increased melting occurred in September.

The highest albedo values are found along the southeast coast of the ice sheet which is consistent with the summer peak of precipitation due to onshore flow loaded with high water vapor content. Peak albedo values are found at an altitude of about 2200 m.a.s.l. The northeastern slope of the ice sheet experiences little precipitation as evidenced by lower albedos.

5.3 Outgoing Longwave Radiation

Since there is no thermal input at the top of the atmosphere, the net longwave radiation balance at the top of the atmosphere is negative throughout the year. Spatial patterns of the longwave flux over the Greenland ice sheet are dominated by topography, where the minimum outgoing longwave radiation occur at the summit and also at the south dome of the ice sheet. Maximum longwave losses occur in June (-293 Wm^{-2}) along the west coast of the ice sheet and minimum losses in December (-151 Wm^{-2}) at the summit.

5.4 Net All-Wave Radiation

Except for the summer months (June-July-August) the net radiation balance at the top of the atmosphere is negative over the entire ice sheet and the ice sheet loses energy at its top boundary. This radiative loss at the top of the atmosphere has to be balanced by energy exchange with the lower latitudes. This is a major driving force in the global climate system. In June, the net radiation balance is slightly positive over the dry snow areas (~ 15 Wm^{-2}) except in the north where the net radiation balance is slightly negative (~ -10 Wm^{-2}). In the wet snow areas during June the net radiation balance increases to values around 100 Wm^{-2} and over the bare ice to values around 200 Wm^{-2}. During the winter months when there is no solar input the net radiation balance is equal to the net longwave radiation balance.

5.5 Time Series at the ETH/CU Camp

The net TOA all-wave radiation for the ETH/CU Camp (69.57° N, 49.29° W) from May 25 1990 - June 29 1991 is shown in Figure 5.1 together with the net short and longwave radiative fluxes. The net TOA shortwave radiation increases from May to July from about 300 to 550 Wm^{-2} and drops to 5 Wm^{-2} in November. It increases again from February to June from about 15 to 400 Wm^{-2}. The maximum occurs in July even though the maximum incoming shortwave at the top of the atmosphere occurs in June. This shows the effect of the drop in surface albedo between June and July due to surface melting. The TOA broadband albedo drops from around 70% in June to

58% in July. Surface albedo values taken from June-August 1990 also show a large drop in albedo between June and July due to the disappearance of the snow cover. The drop in surface albedo therefore obviously outweighs the effect of an increase in cloudiness which occurred from June to July in 1990 which is expected to increase the planetary albedo. June 1991 net shortwave radiation is slightly less than for June 1990 (362 vs. 376 Wm^{-2}) due to a slight increase in albedo which could be a result of greater cloudiness observed in June 1991 than in June 1990. However, the mean June surface albedo values measured at the camp were slightly higher for June 1991 than for June 1990 (74.0% vs. 76.9%) and therefore are probably responsible for the lower June 1991 net shortwave radiation.

The outgoing longwave radiation at the top of the atmosphere is negative throughout the year. It remains almost constant throughout the summer months at around - 290 Wm^{-2}, increasing to - 150 Wm^{-2} in December. The minimum occurs in June. The net longwave radiation curve also shows the days when clouds occurred as sudden decreases in the flux. Notice that the end of May 1990 was cloudy at the camp, but was relatively clear in June, and became cloudy again in July until the middle of August when it became clear again. This is consistent with synoptic observations made during summer 1990 at the CU/ETH camp. Except for the months of June, July and August when the net balance is positive (maximum of 322 Wm^{-2}, average of 102 Wm^{-2}), there is a net loss of energy at the top boundary throughout the year. The minimum -253 Wm^{-2} occurs in November.

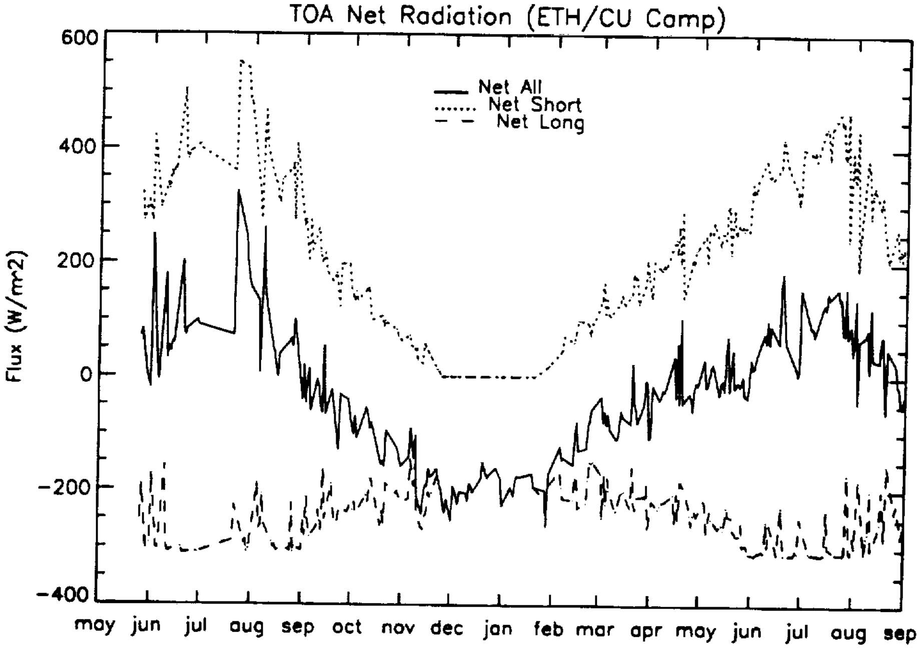

Figure 5.1: Top of the atmosphere radiative fluxes at the ETH/CU camp from May 1990 through August 1991.

5.6 Time Series at the Summit

A similar plot as shown for the ETH/CU camp is shown in Figure 5.2 for 72° 30′ N, 38° W for May 1990 to August 1991. The net TOA shortwave radiation at this location decreases from 267 Wm^{-2} at the end of May 1990 to 12 Wm^{-2} in October. Even though the maximum solar input occurs in June, the maximum net shortwave radiation occurs in July. This is because the planetary albedo at the summit dropped from 71% in June to 68% in July, and even further decreases to 54% in October. In February the planetary albedo rises from 47% to 71% in June 1991. The magnitude of the shortwave radiation balance at the summit is less than that at the ETH/CU camp due to less incoming shortwave energy as well as typically higher surface albedos. However, as mentioned above the planetary albedo at the summit is observed to continually decrease from summer to fall and then rise again from spring to summer. The reason for this is still unclear.

The net TOA longwave radiation again remains negative throughout the year. It decreases from May to July (-241 to -260 Wm^{-2}) and then increases to -135 Wm^{-2} in January. The minimum longwave radiation observed occurred in July (-289 Wm^{-2}) and reflects an increase in cloudiness. The magnitude of the longwave radiation balance at the summit is less than that at the ETH/CU camp due to colder surface temperatures found at the summit.

Again throughout most of the year the net all-wave radiation balance at the top of the atmosphere is negative. The net radiation is slightly positive from May - July (25 - 12 Wm^{-2}), and then becomes negative from August through March. The minimum (-174 Wm^{-2}) occurs in November. Due to less solar input at the summit location vs. the ETH/CU camp, the magnitude of the net radiation during the summer months (June-July-August) is much less (8 Wm^{-2} vs. 98 Wm^{-2}).

In the context of global warming it is important to know the net radiative effect of clouds, which may or may not increase with global warming. Further work will involve computing TOA longwave, shortwave and net cloud forcing for the Greenland ice sheet based on this data.

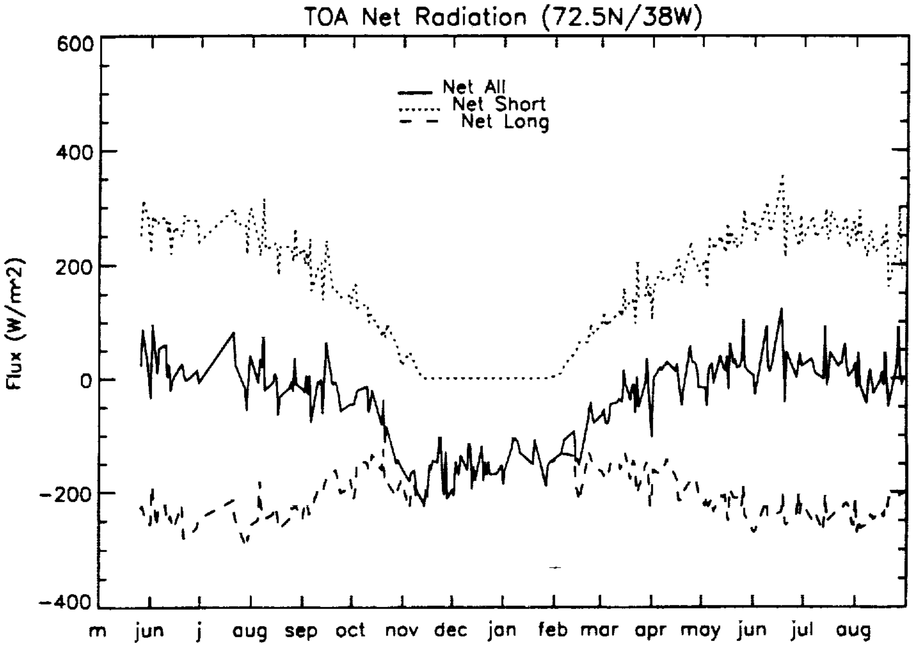

Figure 5.2: Top of the atmosphere radiative fluxes at the summit from May 1990 through August 1991

6. ATSR Case Study

6.1 Introduction

The European Space Agency (ESA) launched the first European Remote Sensing Satellite (ERS-1) in July 1991. The platform is in a sun-synchronous orbit with an inclination of 98.52°, providing near complete polar coverage. ERS-1 carries instrumentation including the Along Track Scanning Radiometer (ATSR) which combines an infrared radiometer and a microwave sounder designed for the measurement of sea surface temperature, cloud top temperature, cloud cover and atmospheric water vapor content. More specifically, the instrument was designed to provide sea surface temperature with an absolute accuracy of 0.5 K or better in conditions of up to 80% cloud cover.

The unique feature of the ATSR instrument is that it observes the Earth's surface through two views. One through a near-vertical atmospheric path (nadir-view) and one at an inclined path of different length (forward-view). Assuming that the atmosphere is horizontally stratified and locally stable during the two minutes it takes the sub-satellite point to reach the along-track point, this technique will permit a more accurate atmospheric correction to be determined than by previous methods. Atmospheric water vapor content information is very sparse over the Greenland ice sheet and data from these two swaths can be combined to retrieve accurate water vapor amounts which are currently not available for the entire ice sheet.

Another feature of the ATSR instrument that makes it particularly suitable for remote sensing of snow covered surfaces is the addition of a channel at 1.6 µm which is very sensitive to water vapor. At this wavelength clouds are more reflective than snow/ice covered surfaces and can be used to distinguish clouds from snow. This is an advantage over other currently used satellite radiometers such as the Advanced Very High Resolution Radiometer (AVHRR) flown on the NOAA-series satellites which currently have no accurate means to differentiate clouds from snow, a problem for Arctic regions which are often covered by clouds.

6.2 Surface Temperature Retrieval

To retrieve snow surface temperatures from thermal infrared (TIR) data requires (1) information on atmospheric conditions such as water vapor and clouds, and (2) precise knowledge of the surface emissivity and its angular behavior.

Previous atmospheric correction methods using thermal infrared channels for clear skies have used the "split-window" approach which uses measurements at two TIR wavelengths (Haefliger et al., 1993). The accuracy of this algorithm to retrieving snow/ice surface temperatures is given at 0.3 K RMS error. Although the multi-wavelength approach is useful for determining the effects of varying water vapor amounts, it is not sensitive to the effects of other atmospheric constituents, such as aerosols. A dual-angle technique can account for the absorption variations due to the different concentrations in all absorbing species. It is this regard that the dual-angle capability of ATSR is expected to give a significant improvement in surface temperature accuracy.

Using the two ATSR views, the surface temperature can then be approximated as

$$T_{surf}=T(nadir)+(-a_1/(a_1-a_2))*[T(nadir) - T(forward)] \qquad (6.1)$$

where T_{surf} is the surface temperature, T(nadir) is the satellite brightness temperature in the nadir view, T(forward) is the satellite brightness temperature in the forward view, $a_1=\sec(\theta_1)$, $a_2=\sec(\theta_2)$, and θ is the satellite viewing angle.

6.3 Application to and ATSR Scene

A first step is to verify that the initial images actually have different brightness temperatures, either because of the different viewing angles or the different channels used. Figure 6.1 shows the comparison on a pixel basis between brightness temperatures measured at 10.8 µm and those measured at 12 µm for a 25 km x 25 km square around the ETH/CU camp on the Greenland ice sheet (69.34° N, 49.17° W) for June 19 1992 at 15:06 GMT. Figure 6.2 compares the temperatures measured at nadir with those measured on the forward scan before and after scan angle emissivity correction at 12 µm. On average, the differences between the 10.8 µm and 12 µm brightness temperatures are 0.57 K for the nadir view and -1.65 K in the forward view for the 25km x 25km area. The temperature difference between the two channels increases with viewing angle due to the greater sensitivity of the 12 µm channel to atmospheric water vapor which increases with increasing path length.

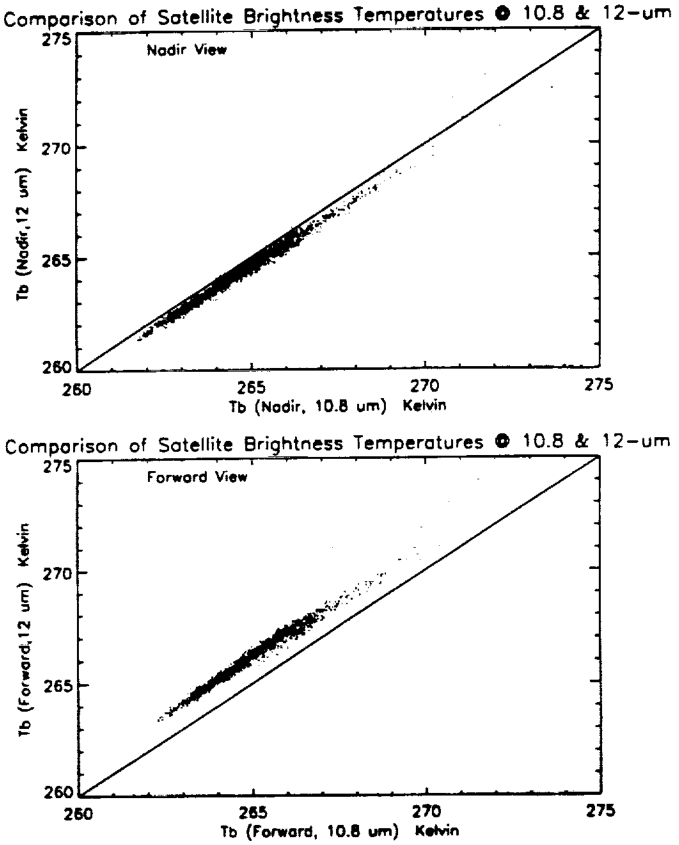

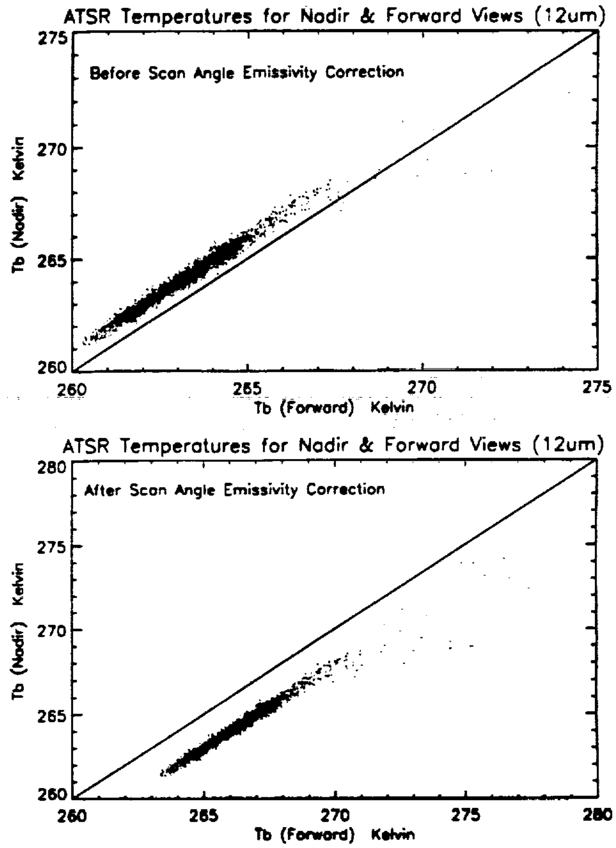

Figure 6.1: June 19, 1992: Comparison of the satellite brightness temperatures measured at nadir and forward in the 10.8 and 12 micron channels for a 25x25km grid centered around the ETH/CU camp.

Figure 6.2: June 19, 1992: Comparison of the satellite brightness temperatures in the 12 micron channel for nadir and forward views for a 25x25km grid centered around the ETH/CU camp. Shown are the brightness temperatures before and after correcting for the variation of emissivity with scan angle.

After correcting the brightness temperatures for scan angle emissivity variations, the remaining brightness temperature differences for the 25km x 25km area are 0.68 K at 10.8 μm and 2.91 K at 12 μm. If there was no atmosphere we should now obtain for a given pixel the same surface brightness temperature for both the nadir and forward images. Therefore, the remaining temperature differences are a result of atmospheric effects, in particular the amount of water vapor in the atmosphere. Notice again the greater temperature differences found at 12 mm are due to its higher sensitivity to atmospheric water vapor. Using the temperature difference between the nadir and forward images could then provide a measure of the total atmospheric water vapor content.

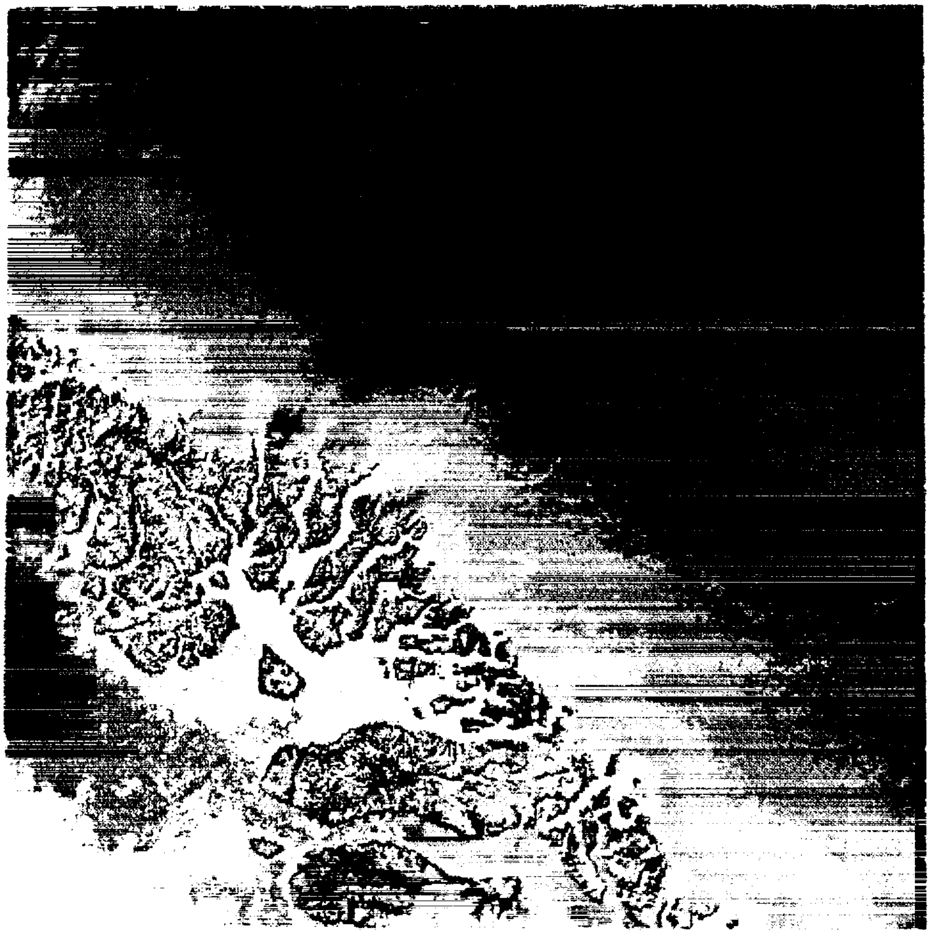

Figure 6.3. Surface temperature as derived from ATSR thermal channels on June 19, 1992.

Figure 6.3 shows the application of equation 6.1 to deriving the surface temperature for June 19 1992. The image shows the Greenland ice sheet near Disko island between 68.48° N and 74.68° N. The purple colors (dark to light) have temperatures from 224-240K, blue colors (dark to light) from 240-252 K, green colors (dark to light) from 253-267 K, yellow from 267.5-269.5 K, orange colors (light to dark) from 270-276 K, and red from 276-280 K. Thus, we can see that on this summer day, the surface temperatures are relatively cold and no melting is occurring along the coast. A few clouds can be seen on the ice sheet in the north and south, as well as a few to the east as evidenced by their colder temperatures. Unfortunately, we have no surface temperature data with which to verify these results. In the future we hope to obtain 1993 ATSR data for which we have ground truth data at the ETH/CU camp.

6.4 Cloud Detection

Thermal imagery is able to detect some clouds over snow/ice using spatial and temporal variations in the temperatures. However, there are many instances where the cloud top temperature is very similar to the surface temperature and can not be detected in the thermal infra-red. The 1.6 µm channel however is very sensitive to atmospheric water vapor and can therefore be used to detect clouds over snow/ice. Typical reflectances for snow at 1.6 µm are around 5%. Thus, for example, the few clouds shown in the June 19, 1992 image have reflectance values around 12%. The 1.6 µm channel can be used not just for cloud detection, but also provide information on the cloud liquid water content, cloud effective radius and optical depth since the cloud reflectance is dependent upon these variables.

6.5 Comparison with AVHRR

Unfortunately, we were unable to find any 1.1 km resolution AVHRR images with which to compare the ATSR images to. However, since the spatial variability of the surface temperature on the ice sheet is relatively small over the footprint of the AVHRR GAC data, the GAC data is used to examine the relative accuracy of the two instruments. Figure 6.4 shows a comparison between ATSR and AVHRR outgoing longwave flux (Wm^{-2}) for 5 clear-sky days over the ETH/CU camp. The mean differences between fluxes is 0.168 W/m^{-2}, standard deviation 2.758 Wm^{-2}. Differences could be due to slightly different viewing geometries and different times of image acquisition. However, in general, the two satellites provide very similar estimates of the longwave flux at the top of the atmosphere.

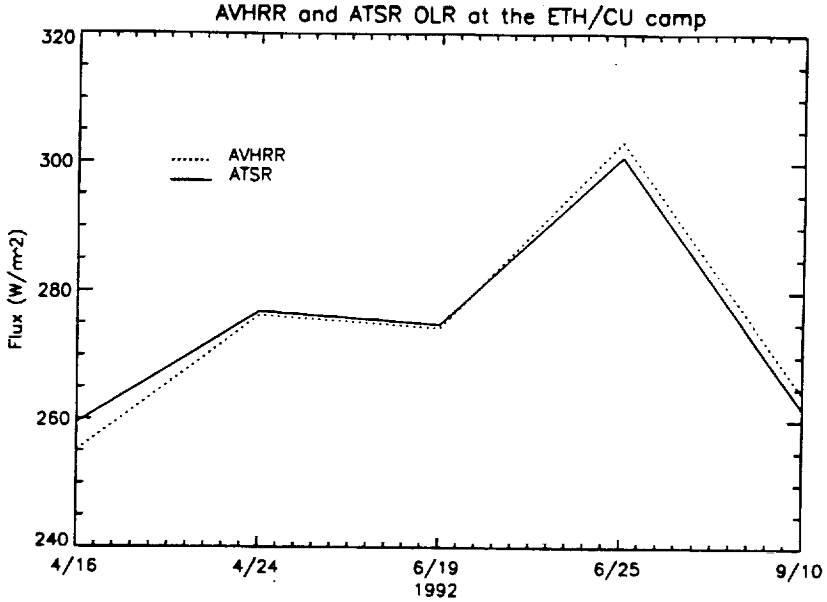

Figure 6.4: Comparison between AVHRR GAC and ATSR derived outgoing longwave flux for 5 clear-sky days at the ETH/CU camp.

7. Surface Melt

The importance of Greenland in the global climate system is largely attributable to the energy exchange between the vast ice sheet and the atmosphere. The nature of this energy exchange varies considerably with the physical state of the snow, as wet snow absorbs approximately 45% more incoming solar energy than dry snow. Therefore, an accurate assessment of the melt extent, both spatially and temporally, is essential for monitoring climatic changes in the polar regions, and for understanding the role of the Greenland ice sheet in the global climate. Using passive microwave satellite observations in conjunction with *in situ* measurements, the extent of melt on the ice sheet can be monitored, and inter-relationships between conditions on the ice sheet and variations in the climate can be studied.

7.1 Surface Observations

Despite the exceptionally warm spring at nearby Jakobshavn, snow melt came particularly late in 1994 at the ETH/CU climate station. As a result, sustained melt did not occur during this year's field season, but prior to our departure from the camp, we set up a thermocouple tower to record temperatures above and below the snow surface during the summer. Temperature data from this tower, along with the coincident radiation data, will provide an indication of the snow melt conditions during our absence. Despite the delay in sustained melt, there were some brief periods of melt in the top 5 cm of snow, which will be of use in interpreting the extent to which shallow melt events influence the passive microwave signal. In addition, observed trends in the near surface snow temperatures and their relationship to snowfall events are expected to provide useful insight to the genesis of melt and the role of albedo in the melt process.

Some interesting relationships were observed between snow temperatures, snow depth, and surface albedo, which are shown in Fig. 7.1. The sharp increases in snow depth are indicative of snowfall events, and as expected, the snowfall is accompanied by significant albedo increases. What is particularly notable is that on each occasion that melt appeared to be imminent, as indicated by the steady rise in snow temperature, fresh snow fell, and the snow temperature decreased. One possible explanation is that these events may be the result of the passing through of low pressure synoptic scale weather systems. However, the climate data from the camp indicate that the period was one of slightly high pressure with the winds primarily being katabatic before and after the snowfall. The skies were clear during the initial warming, but they were cloudy during the brief melt period, and the cooling occurred under cloudy skies after the snowfall when the albedo was highest.

These relationships suggest that the warming that precedes the snowfall events and the cooling that follows are primarily radiatively driven. Insolation increases throughout the spring facilitate snow grain growth, as does night time cloud cover. This grain growth together with the higher sun angles, increases the amount of solar energy absorbed by the snow, and causes the temperatures to rise. After the fresh snowfall, however, the surface albedo is higher (Fig. 7.1) thus reducing the amount of absorbed energy, which in turn decreases the temperatures. It follows then that albedo feedback associated with fresh snowfall can significantly postpone the onset of melt at the ice sheet interior, despite warm weather near the coast. There is an apparent decoupling between the ice sheet interior and the coast, and part of our ongoing research is focused on assessing its extent. The temperature patterns are most likely a result of a combination of radiative effects and weather systems, and to evaluate the relative contributions of each to causing melt will require a detailed analysis of the nearby coastal climate data.

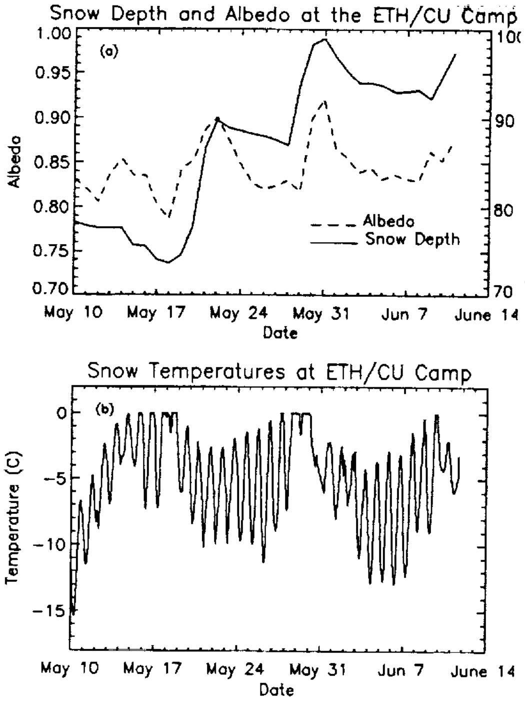

Figure 7.1: Snow depth and albedo (Fig 7.1 top) and snow temperature at 5 cm depth (Fig 7.1 bottom) at the ETH/CU camp for May 10, 1994 - June 11, 1994. The increases in snow depth indicate snowfall events, and associated with these are an increase in albedo, and a decrease in snow temperature in the days that follow the event.

7.2 Passive Microwave Melt Assessment

While melt extent and variability on the ice sheet are still poorly known, recent advances have been made in the use of passive microwave satellite data from the Scanning Multichannel Microwave Radiometer (SMMR) and the Special Sensing Microwave Imager (SSM/I) to estimate these parameters. These include the use of 18 GHz and 19 GHz single-channel threshold techniques (Mote et al., 1993, Zwally and Fiegles, in press, Ridley, 1994), a 37 GHz modeled approach (Mote and Anderson, in press), and methods that employ a combination of channels (Steffen et al., 1993, Abdalati and Steffen, in press). All of these methods are based on the fact that microwave brightness temperatures (T_b) increase dramatically when dry snow becomes wet. This increase occurs because during the transition from dry to wet snow, the dominant scattering mechanism changes from volume scattering to surface scattering. Subsequently the microwave emissivity (e), which relates the physical temperature (T_p) to the brightness temperature by the Rayleigh-Jeans approximation (Eq. 7.1), approaches that of a black body (Matzler and Hueppi, 1989).

$$T_b = eT_p \tag{7.1}$$

These changes in emissivity vary with frequency and polarization, and it is these variations that form the basis for our approach to melt assessment (Abdalati and Steffen, in press). Using a normalized difference between the SSM/I 19 GHz horizontally polarized channel (19H) and the 37 GHz vertically polarized channel (37V), a parameter referred to as the cross-polarized gradient ratio (XPGR) is established as shown in Eq. 7.2 (For the SMMR instrument, the 18 GHz horizontally polarized channel (18H) is used instead of the 19H.). Like the brightness temperatures, the XPGR exhibits a strong melt signal, which, when compared to *in situ* data, allows for the definition of a melt threshold in the signal. An XPGR time series for the ETH/CU camp is shown in Fig. 7.2 along with the dates of melt onset and the melt threshold. This threshold was determined to be XPGR=-0.025, which corresponds to a mean snowpack wetness at the ETH/CU camp of -0.5% by volume.

$$XPGR = \frac{T_b(19H) - T_b(37V)}{T_b(19H) + T_b(37V)} \tag{7.2}$$

where Tb(19H) and Tb(37V) refer to the brightness temperatures of the 19H and 37V channels.

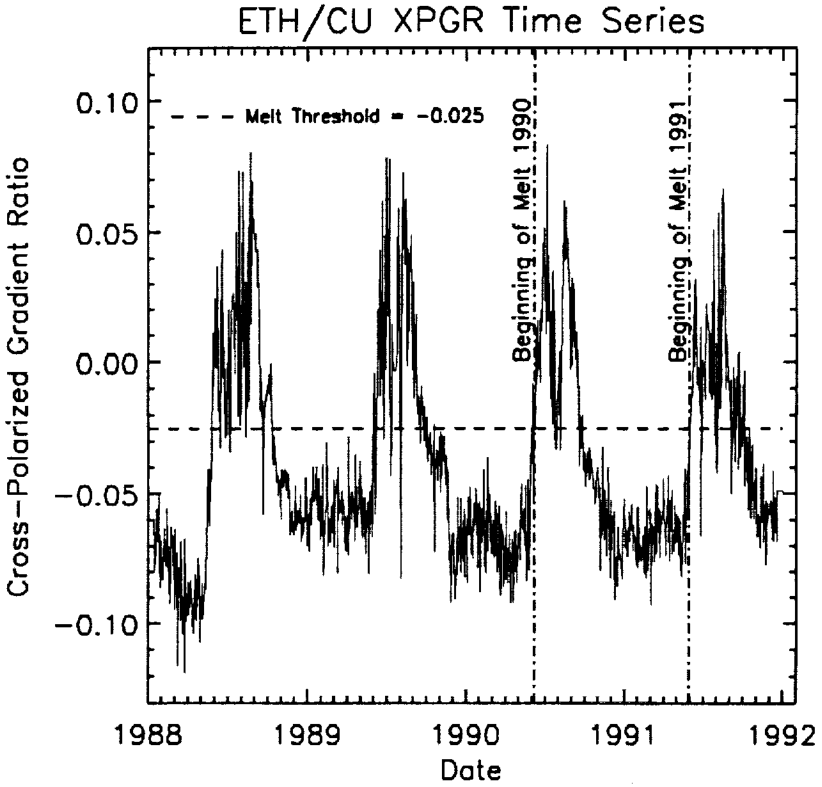

Figure 7.2: SSM/I cross-polarized gradient ratio (XPGR) time series for the ETH/CU station. The melt threshold is shown (horizontal dashed line) along with the two days on which the melt onset occurred at the camp in 1990 and 1991.

Using data sets provided on CD-ROM by the National Snow and Ice Data Center (NSIDC), all available SMMR and SSM/I data from 1978-1991 were examined. For each coverage day and every pixel on the ice sheet, the XPGR was calculated and compared to the melt threshold. Pixels with XPGR values in excess of the threshold on a given day were classified as experiencing melt on that day, while those with values below the threshold were considered to be dry. Using this classification scheme the seasonal melt extent was determined for each year, and it is plotted in Fig. 7.3, which shows a 3.4% increase in mean areal melt extent over the coverage period. Fig. 7.4 depicts the total melt extent for 1983 and 1991, the years of maximum and minimum melt respectively.

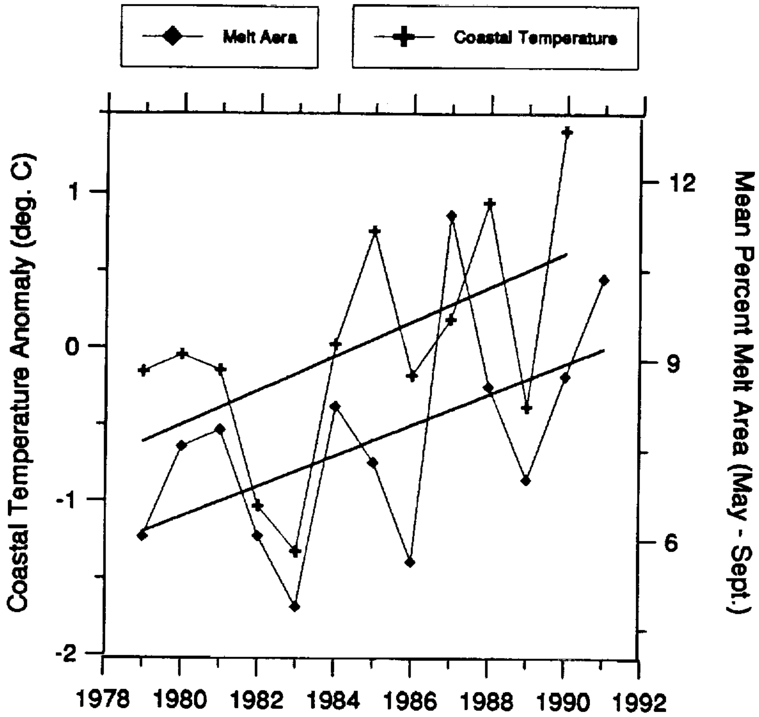

Fig. 7.3: *Mean areal melt extent throughout the melt season (May-September) as derived using the XPGR method. The results show an increasing trend in melt area of 3.4% per year. Total melt extent for the year with minimum melt (1982) and maximum melt (1991). (See cover page)*

7.3 Passive Microwave Melt Algorithms: Limitations

While several methods exist for estimating melt extent from passive microwave satellite observations, each has its own geophysical limitations. The method based on differences between winter and summer SSM/I 19 GHz brightness temperatures (18 GHz in the case of SMMR) has an inherent cold region bias, i.e. it is more likely to predict melt in the cold areas of the ice sheet than in the warm (Abdalati and Steffen, in press). Furthermore, the coupling of summer melt estimates to mean winter brightness temperatures in this approach reduces its applicability to interannual comparisons (Abdalati and Steffen, in press). A potential weakness of the 37 GHz brightness temperature approach in relation to the others is that it is the most sensitive to atmospheric effects.

The primary limitation of the XPGR method arises from the difference in signal emanation depths of the two channels used. When the snow is wet, this difference is on the order of a few centimeters, and the variation in physical temperature (if any exists) is of little consequence in the XPGR. At the time of surface refreeze, however, the temperature gradients and the differing emission depths can potentially result in a melt signal, despite the presence of a frozen surface layer, particularly in the area identified by Benson (1962) as the "soaked zone." This occurs because when cold autumn air begins to freeze the surface of the snowpack, the 37 GHz signal is reduced prior to the 19 GHz signal, which is much more strongly influenced by the warmer subsurface snow. As a result, their normalized difference (XPGR) remains high, even though the surface snow is frozen. For this reason, the estimated dates of refreeze are later when the XPGR method is used than when a single-channel approach is taken.

However, this apparent limitation in surface refreeze identification allows for the detection of wet snow beneath a frozen surface, and can potentially be very useful in facies classification.

Estimates of the end of the 1990 melt season for each pixel were made using both the XPGR method and the method of Mote et al., (1993) in order to determine the time difference in refreeze detection. The results show that the XPGR estimate is consistently later than that of the single-channel, as expected. this time lag is insignificant (5 days or less) in what we believe to be the percolation zone, and significant (greater than 5 days) in what is believed to be the soaked zone (Fig. 7.4).

The presence of an extended time lag in the soaked zone can be attributed to the high thermal inertia of the very wet snow in this region. A large portion of the heat lost from the snowpack in the soaked zone is latent heat, so as the top begins to cool, the deeper layers remain warmer while the liquid water freezes. Thus a strong subsurface temperature gradient is created which sustains the XPGR melt signal. In the percolation zone, however, the thermal inertia is not as high, and more of the energy lost to the colder air is in the form of conductive and sensible heat flux, rather than latent heat flux. Since less of the energy transfer is associated with phase change, the temperature gradient is weaker in the percolation zone. As a result, the XPGR refreeze estimates in these areas agree with the 19 GHz estimates.

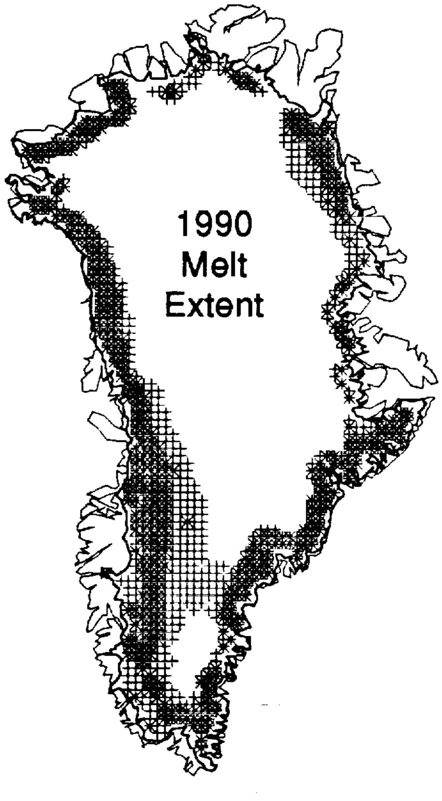

Fig. 7.4: Melt area map showing the difference in end of season refreeze estimates between the single-channel method of Mote et al. (1993) and the XPGR method. The "+" symbol indicate areas to which the refreeze estimates differ by 5 days or less, while the "" symbol indicates the regions where the difference is greater than 5 days. The large differences seem to occur in the soaked zone, while the small differences occur in the percolation areas. This is most likely attributable to the thermal inertia of the soaked zone and the differing penetration depths of the 19H and 37V channels.*

In some portions of the ablation zone, there is also no appreciable difference between the two methods in the refreeze estimates. We believe this to be attributable to the similarity of emission depths of the two channels in solid ice. In other words, since the difference in emission depth between the two frequencies is small, the brightness temperatures are not affected differently by the temperature gradients in the emitting layers.

Each passive microwave-based method of melt detection is impacted by different geophysical phenomena. As a result, a combination of methods is required for a comprehensive assessment of the melt conditions on the ice sheet. Furthermore, the differing emission depths associated with the multi-channel XPGR can potentially enable classification of all four facies of snow on the Greenland ice sheet, thus further improving our ability to monitor changes in the ice sheet's surface and its climate.

8. SMMR and SSM/I-Derived Snow Accumulation

In 1993 we developed a passive microwave radiative transfer model to estimate snow accumulation in the dry snow region of the ice sheet (Steffen et al., 1994). This model still requires considerable refinement to accurately represent the effects of snow accumulation and hoar formation on the microwave signal, but a comparison to ice core data reported by Bolzan and Strobel (1994) show qualitative agreement between our model and field data for the summit. Our current research plans include further development of the model to yield quantitative assessments of snow accumulation.

Our preliminary accumulation estimates along with rough estimates of ablation have been used by geophysical researchers at the University of Colorado and NOAA's Geosciences Laboratory, for initial input into a rheological model. This model, which calculates the elastic and anelastic behavior of the Earth under different loadings, is currently being used to assess the deformation and the geodetic variation of the Earth associated with changes in the mass balance of the Greenland ice sheet. The analysis indicates that the vertical displacement of the Earth's surface caused by these mass balance variations is on the order of a few centimeters over a five year period. Since such a deformation is believed to be detectable with a combination of GPS measurements and high precision gravity measurements, the researchers are planning a collaborative field campaign beginning this year to measure the displacements. Although our mass balance estimates are still very crude, they provide the first reasonable input to the model, and they will be continually be updated as our ability to derive accumulation and ablation improves.

Research efforts in the coming year will be focused on refining the model to include more accurate representation of the snow structure. Primarily this will include parameterizing hoar development based on identification of hoar formation events by the method of Shuman and Alley (1993). When this is done, the model will produce quantitative estimates of snow accumulation in the dry snow region of the ice sheet. These will be compared to the ice core-derived accumulation estimates of Bolzan and Strobel (1994) and the theoretically derived results of Bromwich et al. (1993).

9. REFRACTION AND ICE MOVEMENTS

9.1 Introduction

In continuation of earlier campaigns (1990, 1991) a geodetic program was performed from May 23 to June 23,1994. The participants have been Professor Dr.-Ing. Manfred Stober and Dipl.-Ing. (FH) Jürgen Kreutter, Both members are from the Department of Surveying at the Fachhochschule für Technik in Stuttgart/Germany.

The geodetic research program was financially promoted by the Deutsche Forschungsgemeinschaft (DFG), by Verein Freunde der FHT Stuttgart and by the Department of surveying of FHT Stuttgart. It was supported logistically by the Alfred-Wegener-Institute for Polar and Marine Research (AWI), Bremerhaven/Germany.

Since 1959 geodetic measurements have taken place along an East-West-profile across Greenland with the aim to provide a contribution to the study of the mass balance of the Greenland ice sheet. A very important part in determining the volume of the ice is the knowledge of the surface heights and their temporal change. From this data it is possible to conclude directly the growth or reduction of the ice masses. Several methods of terrestrial height measuring had been applied. In the EGIG-campaigns 1959 and 1968 the geometric leveling was used (Mälzer, 1964, Seckel, 1977a). Since 1987 the Institute for Surveying of the TU Braunschweig (Möller, 1990, Kock, 1993) continued these works with the more economic trigonometric leveling with ranges up to one kilometer. A disadvantage of this method, however, is the source of error "refraction", i.e. that the beam of light between observation point and target does not fallow a strait line. The path the beam of light follows is a curve due to refraction caused by atmospheric density variations.

The main intention of the research program of 1991 and 1994 is to examine more closely, refraction under the special conditions over the Greenland ice surface. Knowledge of the related meteorological parameters of temperature, humidity, wind and radiation are needed. For this reason, collaborations with the Greenland climate field studies of the Geographic Institute of ETH Zürich (1991) and the University of Colorado (1994) were favorable.

The following questions should be investigated; (a) How does the amount of the refraction coefficient above the ice change due to different atmospheric conditions, and ground distances for the beam of light; (b) Is it possible to calculate the refraction coefficient by using meteorological data; (c) Is it possible to determine local differences in the refraction coefficient, which would be necessary to eliminate remaining systematic errors when using the method of simultaneous reciprocal zenith angles?

Another main program is the evaluation of ice movements. According to calculations of Professor Ohmura, ETH, Switzerland, the station was expected to be situated at the equilibrium line. It is of glaciological interest to test this statement and to determine the velocity parameters for this part of the Greenland ice sheet.

The measuring program 1994 was:

- Refraction studies with new temperature measuring device,
- Attachment of the ETH-Camp by GPS to Jakobshavn (June 19,1994),
- Remeasurement of the deformation figure (terrestrial + GPS),
- Reconstruction of old positions from 1990 and 1991 in terrain,
- Remeasurement of old positions 1990 and 1991 in terrain,
- Stratigraphy in snow pits at 4 places.

9.2 Refraction

Zenith angles and distances:

- Simultaneous reciprocal zenith angles along one baseline between points 100 and 200 (length = 950m), measured with opto-mechanical theodolits (WILD T2).
- Electro-optical distance measurement (WILD Di 3000).
- Zenith angles in one direction to a target about 3 m above snow.
- Longitudinal sections of the topography along the baseline by cinematic GPS for determination of the distance between beam of light and ice surface.

Meteorological data :

Together with the trigonometric height measurements vertical temperature profiles were found. For this purpose a new measuring device was used :

- Two temperature masts from FHT Stuttgart, working with 6 ventilated QUAT-sensors up to 3 m above the snow surface.
- Measuring equipment from the University of Colorado Boulder at the camp station (100) with profiles of temperature, wind velocity and direction, and different radiation parameters.

As invented, all geodetic and meteorological measurements could be performed at different weather conditions.

Evaluation methods and previous results:

Simultaneous reciprocal zenith angles. From simultaneous reciprocal zenith angles between two points 1 and 2 we obtain the height difference Dh:

$$Dh = S/2 * (\cos Z1 - \cos Z2) - S^2/ (4R)*(k1 - k2) \qquad (9.1)$$

with S = slope distance, Z1, Z2 = zenith angles on stations 1 and 2, R = earth radius (about 6394 km), r = radius of beam of light, k1, k2 = efficient refraction coefficients in 1 and 2, definition of the refraction coefficient k = R/r.

Only if the efficient refraction coefficients are equal in both stations (k1 = k2) the height difference is free from systematic refraction errors. Under this condition we can obtain the true height difference

$$Dh = S/2 * (\cos Z1 - \cos Z2) \qquad (9.2)$$

and the mean efficient refraction coefficient k for the whole line from

$$k = 1 + R/S * (200 - Z1 - Z2) * \pi/200 \qquad (9.3)$$

Table 9.1: Efficient refraction coefficients k from simultaneous reciprocal zenith angles , line 100 - 200 , distance = 949.86 m height difference stakes = 9.95 m

Jul. Day 1994	Date 1994	Time Camp Time GMT -2 h	Dh (m) Stake	Scale	Refraction Coefficient k Conditions Sunny with wind	w/o wind	Overcast with wind	w/o wind
148	28.05	17.33-19.03	9.975	10.451	0.595			
149	29.05	15.35-16.05	9.951	10.446				-0.004
151	31.05	13.02-16.02	9.950	10.445	0.227			
152	1.06	16.03-19.33	9.942	10.437				0.227
153	2.06	14.32-17.32	9.946	10.441	0.365			
154	3.06	15.03-20.02	9.945	10.440	0.465			
156	5.06	12.33-15.02	9.942	10.437	0.214			
157	6.06	17.02-20.02	9.935	10.431	0.616			
159	8.06	17.32-19.32	9.934	10.430		0.294		
160	9.06	09.35-14.04	9.943	10.438	0.503			
161	10.06	10.32-13.33	9.931	10.426			-0.086	
162	11.06	11.05-14.02	9.930	10.426		0.130		
163	12.06	09.47-13.02	9.926	10.420				-0.076

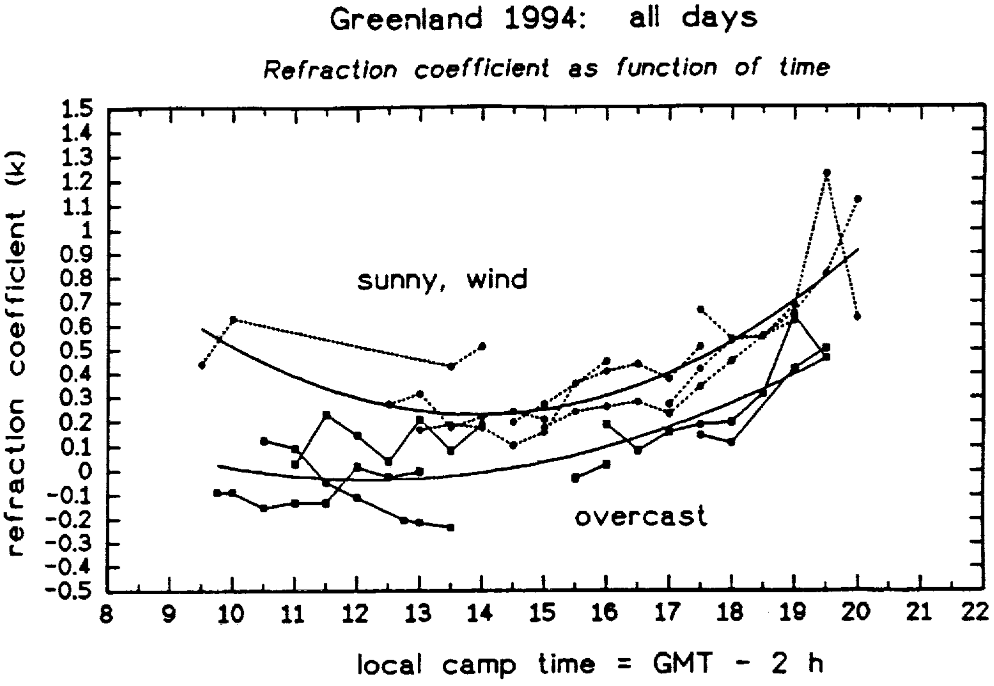

Figure 9.1: *Dependency of refraction coefficient k on local time.*

Results:

- The refraction coefficient k is depended on weather conditions (Table 9.1). The biggest, positive values appear when we have full sun radiation and strong wind. About half of the observed data was taken under these weather conditions.
- Very little or even negative values of k appear when the sky is overcast.
- The refraction coefficient is changing with day time. As we see from the adjusted smoothing parabola (Fig. 9.1), k is minimum at midday and there is a strong increasing of k in the afternoon. So we find a correlation between k and sun rise, even when weather is overcast.
- Apparently k is influenced by those parts of sun radiation which are able to penetrate through thin clouds. This time dependency has to be considered when estimating the correlation between k and various weather conditions.
- Compared to the results from 1991, we now find a smaller range between biggest and smallest k, but the same principal dependency on weather conditions. In 1991, air temperatures had been much higher than in 1994. We also had more humidity from melting processes in 1991 (sometimes slush surface!), what never occurred in the cold summer of 1994.

Local refraction coefficients from vertical temperature profiles

If we accept an atmosphere with globe-symmetric stratification we obtain with the refractive law of SNELLIUS

$$n * \sin Z = \text{const} \tag{9.4}$$

and the local refraction coefficient is given by

$$k = R / r = - \sin Z / n * (dn/dh) \tag{9.5}$$

with Z = zenith angle, n = refractive index, dn/dh = vertical gradient of the refractive index.

From the relationship of BARRELL + SEARS for the refractive index as a function of the meteorological data (t,p,e)

$$n - 1 = a_1 * p/T - a_2 * e/T \tag{9.6}$$

With a_1, a_2 = wavelength dependent coefficients, p = atmospheric pressure [hPa], e = partial water vapor pressure [hPa], T = absolute temperature [K].

we find the local refraction coefficient κ

$$\kappa = 501.525 * \sin Z * p/T^2 * (0.034 + dT/dh) + 79.135 * \sin Z/T * de/dh \tag{9.7}$$

Neglecting the small influence of humidity ,we can apply this method by determining the vertical temperature gradient dT/dh and from that calculate the local refraction coefficient k

$$\kappa = 501.525 * \sin Z * p/T^2 * (0.034 + dT/dh) \tag{9.8}$$

As pointed out before, we had built two new temperature masts, each with ventilated QUAT-sensors in 6 levels up to 3 m above the snow surface. (construction Prof. Dr. Stohrer, FHT Stuttgart). The data were automatically stored by a field computer HUSKY HUNTER 16.

It is of main interest to evaluate possible differences of local refraction at the two ending points of the sight line. So it is very important to know the accuracy of the temperature measuring sensors, especially relative to each other. The intention was to measure the air temperature with a relative accuracy of few K/100.

9.3 Ice movements and deformations

A very important part of the program is the knowledge of surface heights and their temporal change. As for the GPS-receivers, only instruments operating with high resolution on two frequencies were used:

1990 + 1991 : Wild-Magnavox WM 102,
1994 : Leica GPS-System 200.

The displacement is calculated from repeated GPS-positioning. Point C3 was measured in three periods (1990, 1991 and 1994). Another point (A2) was first established in 1991 and remeasured in 1994. All positions have been fixed to the same reference point JAKOBSHAVN by direct simultaneous baselines in 1991 and 1994, but only indirectly by JAKOBSHAVN - CONSTABLE-PYNT - CAMP in 1990.

a) Horizontal ice movements

Flow vector by GPS-measurements

As we see from Table 9.2, azimuth and flow velocity are not exactly agreeing in the periods 90-91 and 91-94, probably due to the weak positioning in 1990. For the best values we have to consider the period average 91 - 94, which is long enough and derived from homogenous GPS-measurements. The same horizontal displacement exists at point A2 (Table 9.3). There is very good agreement in the velocity vector, but the azimuth is a little different (1°). On the whole the general flow vector is toward the Jakobshavn glacier.

Table 9.2: Horizontal displacement at ETH/CU-Camp (C3) 90 - 94

Date	Time interval (day)	Horizontal value (m)	Displacement at c3 velocity (m/day)	Azimuth		
				°	'	"
13.07.90 - 27.07.91	379	121.71	0.3211	236	01	32
27.07.91 -20.08.91	24	7.97	0.3321	232	08	05
20.08.91 - 19.06.94	1031	320.49	0.3109	234	31	24
13.07.90 - 19.06.94	1434	450.14	0.3139	234	53	21
Average 91:19.06.94	**1043**	324.49	**0.3111**	**234**	**28**	**59**
				= 260.54 gon		

Table 9.3: Horizontal displacement at ETH/CU-Camp (A2) 91-94

Date	Time interval (day)	Horizontal value (m)	Displacement at A2 velocity (m/d)	Azimuth		
				°	'	"
Mean 91: 19.06.94	1043	326.68	0.3132	233	35	17
				= 259.54 gon		

Deformations in a terrestrial network

It was possible to find all 4 points from the network of 1991 and measure the deformation network by GPS and terrestrial methods as well. The ranges of the network are in the order of 1 km (Fig. 9.2). By transformation and calculation in the same local coordinate system, we obtain displacement vectors for all 4 points (Table 9.4).

Table 9.4: Horizontal displacements 1991 - 1994 in a terrestrial network

Point	Displacement of point from 1991 to 1994		Discrepancies average - individual	
	range (m)	azimuth (gon)	range (m)	azimuth (gon)
A2	326.56	259.4983	-1.89	+0.1037
B2	321.87	258.9277	+2.80	+0.6743
C2	324.64	260.1933	+0.03	-0.5913
D	325.60	259.7888	-0.93	-0.1868
average	324.67	259.6020		

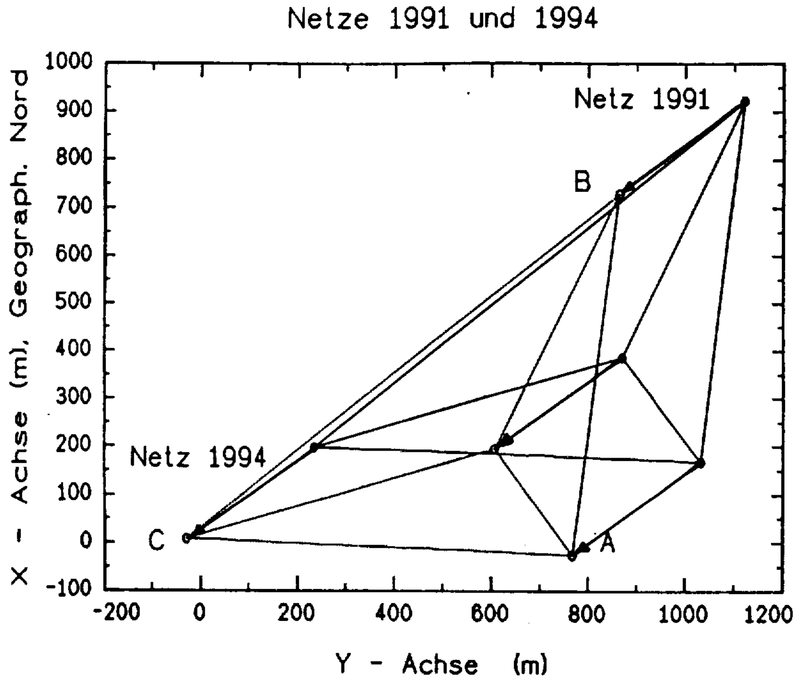

Figure 9.2: Deformation figure and horizontal displacements 1991 - 1994

Conclusions:

- the average displacement 324.67 m (corresponding to 0.3196 m/day) is very good agreement with the results from GPS.
- velocities and flow azimuths are not completely homogeneous. Each point has individual values, so local effects (surface topography and/or bedrock topography) may have great influence.
- the differences are significant, because the measuring accuracy is much better (order of 1 cm) in relation to the big displacements.

Table 9.5: Distortions in the network 1991 - 1994

From	To	Length 91 (m)	Length 94 (m)	Change of length 94 - 91		
				(m)	ppm	ppm/day
C2	A2	798.012	797.860	-0.152	-190	-0.19
C2	B2	1146.762	1148.848	+2.086	+1816	+1.79
B2	A2	760.262	761.592	+1.330	+1746	+1.72
D	A2	271.768	272.372	+0.604	+2118	+2.08
D	B2	592.613	593.846	+1.233	+2076	+2.04
D	C2	663.490	663.468	-0.022	-33	-0.03

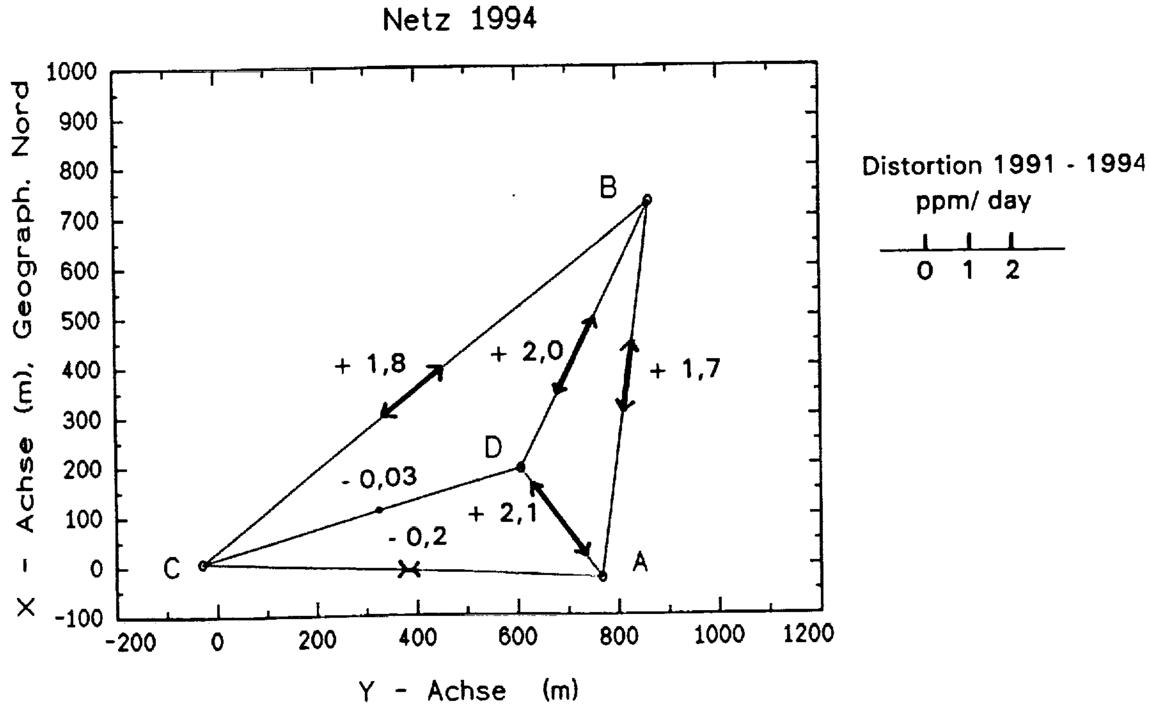

Figure 9.3: Distortions in the network 1991 - 1994

Comparing the changes of length in the deformation network, we also find individual distortions of ranges (Table 9.5). The flow azimuth coincides approximately with direction B-C, but the distortions along and across this azimuth are almost equal. On the other hand, lines in about the same azimuth (C-B, C-D) do not show the same distortion, all the distortions are individual ones. There are even some ranges (D-C and A-C) remaining unchanged. Due to this inhomogeneous behavior no strain rates were calculated.

b) Vertical ice movements

Height changes at the same place

For all questions concerning the mass balance the change of height at the same position is very important. For this purpose the old positions from 1990 and 1991 of point C3 were reconstructed in the field. This was only possible by using previous values of the deformation rate and azimuth. Only now, after evaluation of the actual displacement vector, are we able to define the true old positions. In order to correct the previous heights, a topographic map was made for the supposed area, from which the exact heights could be found by interpolation.

In order to determine the snow accumulation, snow pits were dug at 4 positions: C2(94), C2(91), A2(94), and D(94). At positions C2 and D the original wooden stick was found, so the old snow horizon was well known. The stratigraphy is shown in figure 6.

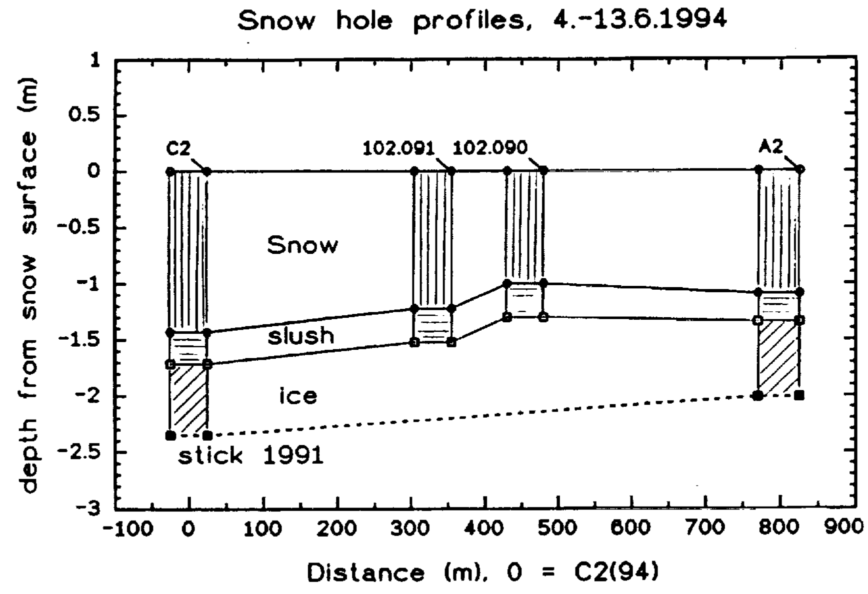

Figure 9.4: Stratigraphy of snow pits 1994

Combining the GPS-heights at the snow surface and the data from the snow pits we are able to give absolute heights for all snow and ice horizons. For this presentation all the heights are related to Jakobshavn with ellipsoidal height JAV = 52.093 m, which is not the true ellipsoidal height, but a fixed value for all height comparisons.

The results are shown in Table 9.6. The most important value is the ice horizon, because the snow surface might be disturbed by local and seasonal effects. From 1990 to 1994 the ice height decreased -2.68 m. In the period 1990 to 1991 there was a decrease of -0.59 m. Based on this data we can infer that there was a level decrease of .67m per year for 1990 to 1991, and a decrease of .2m per year between 1991 and 1994. The big difference between the two periods is probably effected by the bad height determination in 1990 (indirectly via Constable Point). But in 91 and 94 we had homogeneous and short GPS baselines with good results, so we can suppose a height diminution in the last 3 years of -0.20 m/year. This agrees well with those from the EGIG-line (Kock, 1993), but contradicts the results from satellite altimetry which gave increasing ice values of +0,3 m/year (Zwally, 1989).

Table 9.6: Height changes of snow and ice at the same position

Position of C3 at date	Height changes (m)				Vertical velocity of ice = change of height per year	
	94 to 90		94 to 91			
	snow	ice	snow	ice	94 - 90	94 - 91
Mittel 91			+0.09	-0.59		-0.20
7/90	-1.58	-2.68			-0.67	

Vertical ice flow

The vertical component of ice flow is derived by observation of the moving wooden stakes, which were found at the two points C2 and A2 from 1991. In 1991 they had been established in surface horizon, and in 1994 they were found 0.65 m below the actual ice horizon. All heights (in relation to the fixed point JAV = 52.093 m) of the moving stakes are shown in Figures 9.5 and 9.6. We obtained the results :

<u>Vertical ice flow at point C2/C3:</u>

height difference of stick in flow direction = - 5.73 m ,
surface slope inclination (measured) = - 4.34 m

vertical movement, free from inclination = - 1.39 m.

<u>Vertical ice flow at point A2:</u>

height difference of stick in flow direction = - 4.22 m ,
surface slope inclination (approximately) = - 3.0 m

vertical movement, free from inclination = - 1.22 m.

At both places (A,C) the vertical movement of the stake is greater than the height change effected by slope. Therefore the flow vector has a downward trend and the model of rising ice layers cannot be confirmed for this part of the Greenland ice sheet. Together with the large accumulation of snow and new ice over the old stakes we see that the ETH/CU-camp is not situated at the equilibrium line, as expected by Ohmura 1991.

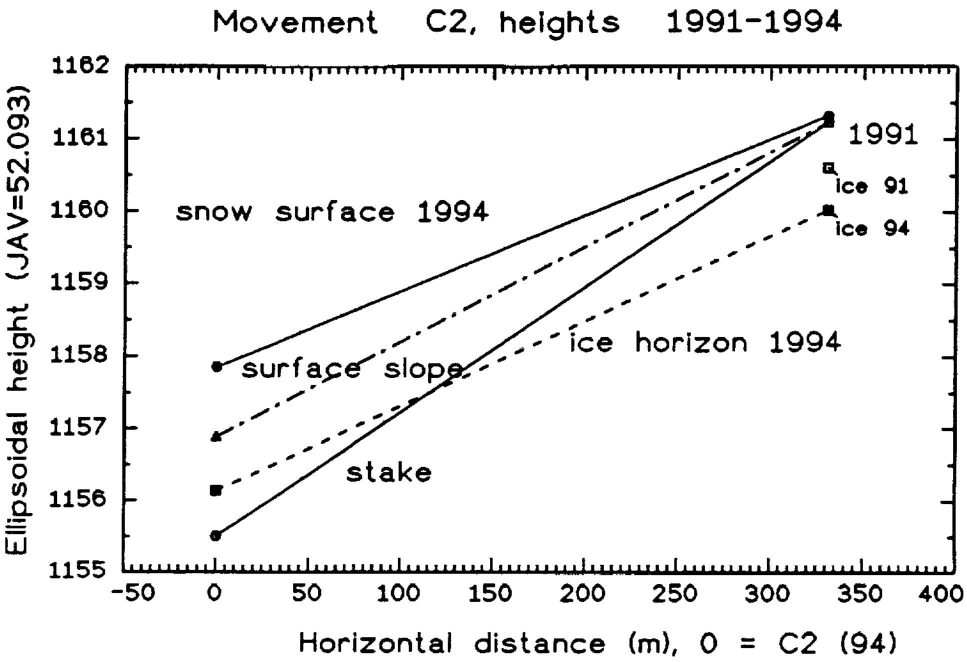

Figure 9.5: Height changes of point C2/C3 (1991 - 1994)

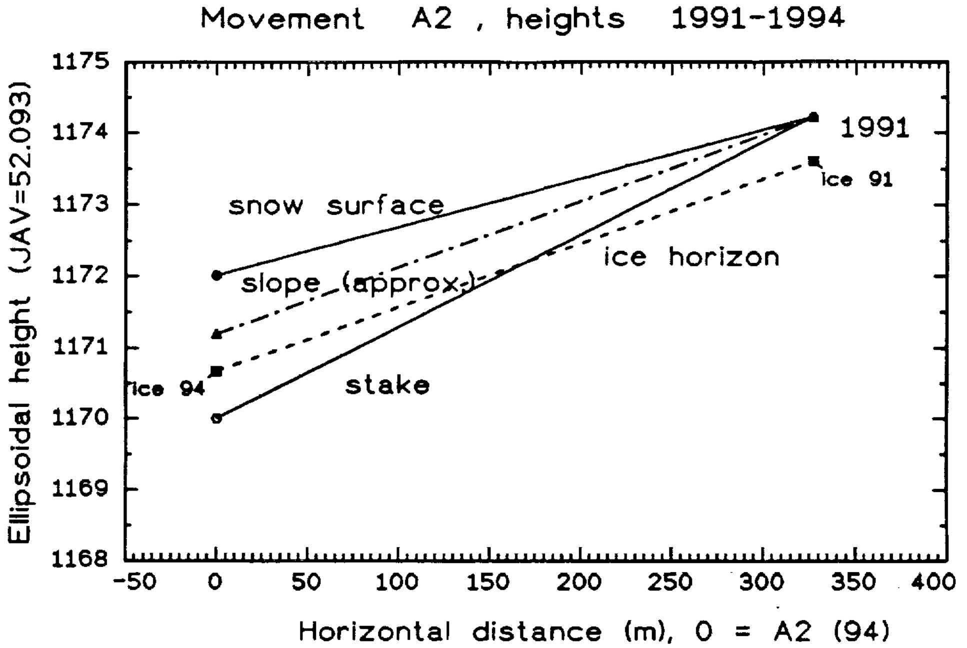

Figure 9.6: Height changes of point A2 (1991 - 1994)

10. REFERENCES

Benson, C.S., Stratigraphic studies in the snow and firn of the Greenland Ice Sheet, U.S. Snow, Ice and Permafrost Research Establishment, Research Report 70, 1962.

Bromwich, D.H., Robasky, F.M., Keen, R.A. and Bolzan, J.F., Modeled variations of precipitation over the Greenland ice sheet, Journal of Climate, Vol. 6, July, 1993.

Bohren C.F., and Beschta R.L., Snowpack albedo and snow density, Cold Reg. Sci. Tech., vol. 1, pp. 47-50, 1979.

Bolzan, J.F. and Strobel, M., Accumulation-rate variations around Summit, Greenland, Journal of Glaciology, Vol. 40, No. 134, 1994.

Colbeck, S.C., Theory of the metamorphism of wet snow, Tech. Rep. Research Report No. 313, U.S. Army Cold Regions Research and Engineering Laboratory, Hanover, NH, 1973.

Colbeck, S.C., Theory of metamorphism of dry snow, J. Geophys. Res., vol. 88, pp. 5475-5482, 1983.

Dodson, A.H., und ZAHER, M., Refraction Effects on Vertical Angle Measurements, Survey Review Vol. 28, 217, 1985 .

Haefliger, M., Steffen, K., Fowler, C., AVHRR surface temperature and narrow-band albedo comparison with ground measurements for the Greenland ice sheet, Annals of Glaciology, 17, 49-54, 1993

Jordan, R., A one-dimensional temperature model for a snow cover: technical documentation for sntherm.89, Special Report 91-16, U.S. Army Corps of Engineers, Cold Regions Research and Engineering Laboratory, Hanover, NH, 1991.

Kock, H., Height determination along the EGIG line and in the GRIP area. Mass balance and related topics of the Greenland ice sheet, 3rd workshop Dec. 1992, GGU Open File Series 93/5, 1993.

Li, Z., Leighton, H.G., Narrowband to broadband conversion with spatially autocorrelated reflectance measurements, Journal of Applied Meteorology, 31, 421, 1992.

Mälzer, M., Das Nivellement über das grönländische Inlandeis der Internat. Glaziologischen Grönland-Expedition 1959, Medd. om Grönländ, Bd. 173, Nr. 7, Kopenhagen, 1964.

Matzler, C.H., and Hueppi, R., Review of signature studies for microwave remote sensing of snowpacks, Adv. Space Research, 9(1), 253-265, 1989.

Möller, D., Geodätische Beiträge zum Massenhaushalt und zur Dynamik des grönländischen, Inlandeises (Zusammenfassung), Jahrbuch Braunschweigische Wiss. Gesellschaft, 1990.

Mote, T.L., Anderson, M.R., Kuivinen, K.C., and Rowe, C.M., Passive microwave-derived spatial and temporal variations of summer melt on the Greenland ice sheet, Annals of Glaciology, 17, 233-238, 1993.

Mote, T.L., and Anderson, M.R., Variations in snowpack melt on the Greenland ice sheet based on passive-microwave measurements, Journal of Glaciology, in press.

Ohmura, A., et al., ETH Greenland Expedition, Progress Report No. 1, Department of Geography, ETH Zürich, March 1991.

Ridley, J., Surface melting on Antarctic Peninsula ice sheet detected by passive microwave sensors, Geophys. Res. Let., 20(23), 2639-2642, 1993.

Seckel, H., Das geometrische Nivellement über das grönländische Inlandeis der Gruppe Nivellement A der Internationalen Glaziologischen Grönländ-Expedition 1967-68, Medd. om Grönländ, Bd. 187, Nr. 3, Kopenhagen, 1977a.

Seckel, H., Höhenänderungen im Grönländischen Inlandeis zwischen 1959 und 1968, Medd. om Grönländ, Bd. 187, Nr. 4, Kopenhagen, 1977.

Shuman, C.A. and Alley, R.B., Spatial and temporal characterization of hoar formation in central Greenland using SSM/I brightness temperatures, Geophysical Research Letters, Vol. 20, No. 23, pp. 2643-2646, 1993.

Stamnes, K., Tsay, S., Wiscombe, W., and Jayaweera, K., Numerically stable algorithm for discrete-ordinate-method radiative transfer in multiple scattering and emitting layered media, App. Opt., vol.27, pp. 2502-2509, 1988.

Steffen, K., Abdalati, W., and Stroeve, J., Climate sensitivity studies of the Greenland ice sheet using satellite AVHRR, SMMR, SSM/I, and in situ data, Meteorology and Atmospheric Physics, 51, 239-258, 1993.

Steffen, K., Abdalati, W., Stroeve, J., and Key, J., Assessment of climate variability of the Greenland ice sheet: integration of in situ and satellite data, NASA progress report, 1994.

Warren, S.G., Optical constants of ice from the ultraviolet to the microwave, App. Opt., vol. 23, pp. 1206-1225, 1984.

Webb, E.K., Temperature and Humidity Structure in the Lower Atmosphere, In :F.K. Brunner, (Editor): Geodetic Refraction, Springer-Verlag, 1984.

Zwally, H.J., Growth of the Greenland Ice Sheet: Measurement/Interpretation, Science, Vol. 246, 1989.

Zwally, H.J., and Fiegles, S., Extent and duration of Antarctic surface melting, J of Glaciology, vol 40, pp. 463-476, 1994.